

1 **The retrieval of snow properties from SLSTR/**
2 **Sentinel-3 - part 1: method description and sensitivity**
3 **study**

4 **Linlu Mei¹, Vladimir Rozanov¹, Christine Pohl¹, Marco Vountas¹, John P.**
5 **Burrows¹**

6 ¹ Institute of Environmental Physics, University of Bremen, Germany

7
8 **Abstract**

9 The eXtensible Bremen Aerosol/cloud and surfaceE parameters Retrieval (XBAER) algorithm
10 has been designed for the Top-Of-Atmosphere reflectance measured by the Sea and Land
11 Surface Temperature Radiometer (SLSTR) instrument onboard Sentinel-3 to derive snow
12 properties: Snow Grain Size (SGS), Snow Particle Shape (SPS) and Specific Surface Area (SSA)
13 under cloud-free conditions. This is the first part of the paper, to describe the retrieval method
14 and the sensitivity study. Nine pre-defined SPSs (aggregate of 8 columns, Drontal, hollow
15 bullet rosettes, hollow column, plate, aggregate of 5 plates, aggregate of 10 plates, solid bullet
16 rosettes, column) are used to describe the snow optical properties. The optimal SGS and SPS
17 are estimated iteratively utilizing a Look-Up-Table (LUT) approach. The SSA is then
18 calculated using another pre-calculated LUT for the retrieved SGS and SPS. The optical
19 properties (e.g., phase function) of the ice crystals can reproduce the wavelength-
20 dependent/angular-dependent snow reflectance features, compared to laboratory measurements.
21 A comprehensive study to understand the impact of aerosol, SPS, ice crystal surface roughness,
22 cloud contamination, instrument spectral response function, snow habit mixture model, and
23 snow vertical inhomogeneity on the retrieval accuracy of snow properties has been performed
24 based on SCIATRAN radiative transfer simulations. The main findings are (1) Snow angular
25 and spectral reflectance feature can be described by the predefined ice crystal properties only
26 when both SGS and SPS can be optimally and iteratively obtained; (2) The impact of ice crystal
27 surface roughness plays minor effects on the retrieval results; (3) SGS and SSA show an inverse
28 linear relationship; (4) The retrieval of SSA assuming non-convex particle shape, compared to

29 convex particle (e.g. sphere) shows larger results; (5) Aerosol/cloud contamination due to
30 unperfected atmospheric correction and cloud screening introduces underestimation of SGS,
31 “inaccurate” SPS and overestimation of SSA; (6) The impact of instrument spectral response
32 function introduces an overestimation on retrieved SGS, an underestimation on retrieved SSA
33 and no impact on retrieved SPS; (7) The investigation, by taking a ice crystal particle size
34 distribution and habit mixture into account, reveals that XBAER retrieved SGS agrees better
35 with the mean size, rather than the mode size for a given particle size distribution.

36

37 **1 Introduction**

38 Snow properties such as snow albedo, Snow Grain Size (SGS), Snow Particle Shape (SPS),
39 Specific Surface Area (SSA), snow purity (Warren and Wiscombe, 1980; Painter et al., 2003;
40 Hansen and Nazarenko, 2004; Taillandier et al., 2007; Gallet et al., 2009; Battaglia et al., 2010;
41 Gardner et al., 2010; Domine et al., 2011; Liu et al., 2012; Qu et al., 2015; Baker et al., 2019;
42 Pohl et al., 2020a) show large variabilities temporally and spatially (Kukla et al., 1986). They
43 play important roles in the global radiation budget, which is critical to some well-known
44 phenomenon such as the Arctic amplification (Serreze and Francis, 2006; Domine et al., 2019).
45 Satellites offer an effective way to understand the surface-atmosphere processes and
46 corresponding feedback mechanisms on the regional, continental and/or global scales (Konig
47 et al., 2001; Pope et al., 2014). Satellite derived snow products (e.g., SGS, SPS, and SSA) are
48 particularly important for short-term hydrological, meteorological and climatological
49 modelling (Livneh et al., 2009). A high-quality snow property data product can also be applied
50 to derive Aerosol Optical Thickness (AOT) over cryosphere (Mei et al., 2020a). High-quality
51 satellite derived snow products and their by-products are also important for the creation of long-
52 term “Climate Data Records“ (SSMC, 2014), which enable a better investigation and
53 interpretation concerning global climate change (Konig et al., 2001). However, both the
54 definition and the corresponding data accuracy of SGS are poor (Langlois et al., 2020) while
55 there is no existing SPS satellite product. The lack of good information on SGS and SPS leads
56 to low quality of SSA (Gallet et al., 2009). The accuracy of SGS, SPS and SSA limits the model

57 performance for the prediction of snow properties related to climate change issues. Lack of
58 information of SGS and SPS also restricts the accuracy of snow bidirectional reflectance
59 estimation, which further limits the retrieval possibilities of aerosol and cloud properties above
60 snow (Mei et al., 2020a, 2020b).

61 A comprehensive overview of remote sensing of SGS, SPS, and SSA can be found in
62 many previous publications (e.g., Li et al., 2001; Stamnes et al., 2007; Koren, 2009; Lyapustin
63 et al., 2009; Dietz et al., 2012; Wiebe et al., 2013; Frei et al., 2012; Mary et al., 2013;
64 Kokhanovsky, et al., 2019; Xiong et al., 2018). The variation of SGS leads to the large
65 variability of Top Of Atmosphere (TOA) reflectance in NIR/SWIR spectral ranges while SPS
66 shows a strong impact on TOA reflectance at visible channels (Warren and Wiscombe, 1980).
67 Different retrieval algorithms have been developed for different instruments. For instance, the
68 MODIS Snow Covered-Area and Grain size (MODSCAG) retrieval algorithm and Multi-Angle
69 Implementation of Atmospheric Correction (MAIAC) algorithm have been used to derive SGS
70 using MODIS and VIIRS instruments (Painter et al., 2003; 2009; Lyapustin et al., 2009).

71 Snow particle shape is another important parameter which affects the estimation of snow
72 properties, such as albedo (Räisänen et al., 2017; Flanner and Zender, 2006), because ice
73 crystals with different shapes have different optical properties (Jin et al., 2008; Yang et al.,
74 2013). The absorption and extinction cross-sections of an ice crystal can be described as a
75 function of size, shape, and refractive index at a given wavelength (van de Hulst 1981;
76 Mischenko et al., 2002 and references therein). Natural snow consists of grains, depending on
77 temperature, humidity, and meteorological conditions, which have numerous different shapes
78 (Nakaya, 1954). SPSs have been classified into different categories, the classification has been
79 increased from 21 (Nakaya and Sekido, 1938) to 121 categories (Kikuchi et al., 2013). Although
80 spherical shape assumption is typically used for field measurements (Flanner and Zender, 2006;
81 Donahue et al., 2020), this approximation is not recommended to be used in retrieval algorithms
82 of satellite measurements because it leads to large differences between observed and simulated
83 wavelength-dependent snow bidirectional reflectance, especially at visible wavelengths
84 (Leroux and Fily et al., 1998; Aoki et al., 2000; Jin et al., 2008; Dumont et al., 2010; Libois et
85 al., 2013). Improper wavelength-dependent snow bidirectional reflectance caused by a

86 predefined SPS leads to low-quality satellite retrieval results. Some attempts to derive SPS in
87 the ice cloud can be found in previous publications (McFarlane et al., 2005; Cole et al., 2014).

88 According to Legagneux et al., (2002), SSA is defined as the surface area of ice crystal
89 per unit mass, i.e., $SSA = A_t/\rho V$, where A_t and V are total surface area and volume, respectively,
90 ρ is the ice density. SSA includes information on both SGS and SPS and it is often used to
91 describe the surface area available for chemical processes (Taillandier et al., 2007; Domine et
92 al., 2011; Yamaguchi et al., 2019). SSA is reported to have a good relationship with snow
93 spectral albedo at the short wave infrared wavelengths (Domine et al., 2007). Optical methods
94 are routinely used to measure SSA in the field (Gallet et al., 2009). Empirical equations have
95 been proposed to describe the change of SSA (Legagneux and Domine, 2005; Taillandier et al.,
96 2007). Few attempts have been made to derive SSA from satellite observations (Mary et al.,
97 2013; Xiong et al., 2018).

98 This paper presents a new retrieval algorithm to derive SGS, SPS, and SSA from satellite
99 observations. In a snow-atmosphere system, satellite observed TOA reflectances are affected
100 by numerous snow and atmospheric parameters. The parameters, which will be estimated in the
101 framework of the eXtensible Bremen Aerosol/cloud and surface parameters Retrieval (XBAER)
102 algorithm, will be called the target parameters. Other parameters, which the TOA reflectance
103 also depends on, will be called the model parameters. In the case of the XBAER algorithm, the
104 target parameters are SGS, SPS, and SSA, whereas the model parameters are aerosol loading,
105 cloud optical thickness, and gaseous absorption. Throughout the paper, SGS will be
106 characterized by an effective radius. Following Baum et al., (2011), the effective radius is
107 defined as $3V/(4A_p)$, where V and A_p are the volume and average projected area, respectively.
108 As can be seen, in the case of a spherical particle, the effective radius is equal to the radius of
109 the sphere. The general concept of the retrieval algorithm is to use simultaneously spectral and
110 angular reflectance measurements, which are sensitive to SGS and SPS. The spectral channels
111 used in the XBAER algorithm are 0.55 μm and 1.6 μm . Both nadir and oblique observation
112 directions from SLSTR are used. An optimal SGS and SPS pair is achieved by minimizing the
113 difference between measured and simulated atmospheric-corrected surface reflectances. SSA
114 is then calculated based on the retrieved SGS and SPS. Nine predefined SPSs (aggregate of 8

115 columns, droxtal, hollow bullet rosettes, hollow column, plate, aggregate of 5 plates, aggregate
116 of 10 plates, solid bullet rosettes, column) (Yang et al., 2013, see Table 1) are used to describe
117 the snow optical properties and to simulate the snow surface reflectance at 0.55 and 1.6 μm at
118 two observation angles.

119 Three points we would like to emphasize to avoid misunderstandings between snow
120 science community and remote sensing community.

121 ➤ **Usage the Yang et al (2013) database for ice crystal in the air (ice cloud) and on**
122 **the ground (snow).** The optical properties of ice crystals presented by Yang et al.,
123 (2013) have been widely used to study ice clouds. In recent publications, it has been
124 demonstrated that they can also be used for snow studies (Räisänen et al, 2015;
125 Pirazzini et al., 2015; Saito et al., 2019; Schneider et al., 2019; Pohl et al., 2020b). In
126 fact, the single-scattering properties of ice crystals in Yang et al., (2013) database are
127 determined solely by given particle size, shape, and refractive index. They can be
128 used to describe the optical properties of both snow particles and ice cloud particles
129 when the particle models represent the aforementioned optical/physical properties
130 (Saito et al., 2019; Personal communication with Dr. Saito).

131 ➤ **Snow particle shape observed from field measurements and derived from**
132 **satellite observations.** For scientists working in a laboratory or on campaign-based
133 studies, the best way to get an image of snow is to use an X-ray microtomography or
134 confocal scanning optical microscope/scanning electron microscope (Hagenmuller et
135 al., 2016; Baker et al., 2019; Personal communication with Dr. Ian Baker). In a field
136 measurement and its related application areas (e.g., calculation of snow albedo), a
137 spherical shape assumption is widely used because it is easier to derive other snow
138 properties such as SSAs and snow albedo based on this assumption, compared to
139 other more complicated shapes (see Appendix). The assumption of spherical and non-
140 spherical shape has much less impact on the estimation of snow albedo compared to
141 the bidirectional reflection features of snow (Grenfel and Warren, 1999; Dumont et
142 al., 2010). Because SPS has a significant impact on the ice crystal phase function

143 while it has a relatively weak impact on the snow extinction/absorption coefficient
144 (Jin et al., 2008). However, the spherical shape cannot be used to provide typical
145 bidirectional reflection features of snow with required accuracy (Jin et al., 2008;
146 Dumon et al., 2010; Jiao et al., 2019), which is the fundamental basis to derive snow
147 properties from satellite remote sensing techniques. Thus, more complicated SPSs,
148 such as those proposed by Yang et al (2013), are recommended to use in the
149 simulations of the angular distribution of snow reflectance. Besides, both snow albedo
150 and directional reflectance are affected by other factors such as how single particle
151 aggregates;

152 ➤ **SGS and SSA.** Although the definition of snow grain constitutes is an ongoing debate
153 in different communities, SGS and SPS are two fundamental inputs for any radiative
154 transfer model, which is the basis for the satellite retrievals (Langlois et al., 2020).
155 Typically, the SSA is more preferable within the snow science community because
156 SSA is commonly used in further applications based on field measurements. We note,
157 however, according to the definition of SSA, for a given SPS, a unique relationship
158 between SGS and SSA can be derived. SPS is the intermediate but fundamental
159 parameter needed to retrieve SSA in our XBAER algorithm.


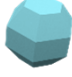







160 This paper is structured as follows: observations characteristics of SLSTR and the
161 laboratory measurements used for sensitivity studies are described in section 2. The theoretical
162 background and the ice crystal database (Yang et al., 2013) are presented in section 3. Section
163 4 describes the eXtensible Bremen Aerosol/cloud and surfaceE parameters Retrieval (XBAER)
164 algorithm. The results of a comprehensive sensitivity study using SCIATRAN (Rozanov et al.,
165 2014) simulations are presented in section 5. The conclusions are given in section 6.

166

167

168

169 Table 1 Snow particle shape provided in Yang et al (2013) database. The abbreviations are
 170 introduced here will be used later

Snow particle shape	Abbreviation	Schematic drawing
Aggregate of 8 columns	col8e	
Droxtal	droxa	
Hollow bullet rosettes	holbr	
Hollow column	holco	
Plate	pla_1	
Aggregate of 5 plates	pla_5	
Aggregate of 10 plates	pla_10	
Solid bullet rosettes	solbr	
Column	solco	

171

172

173

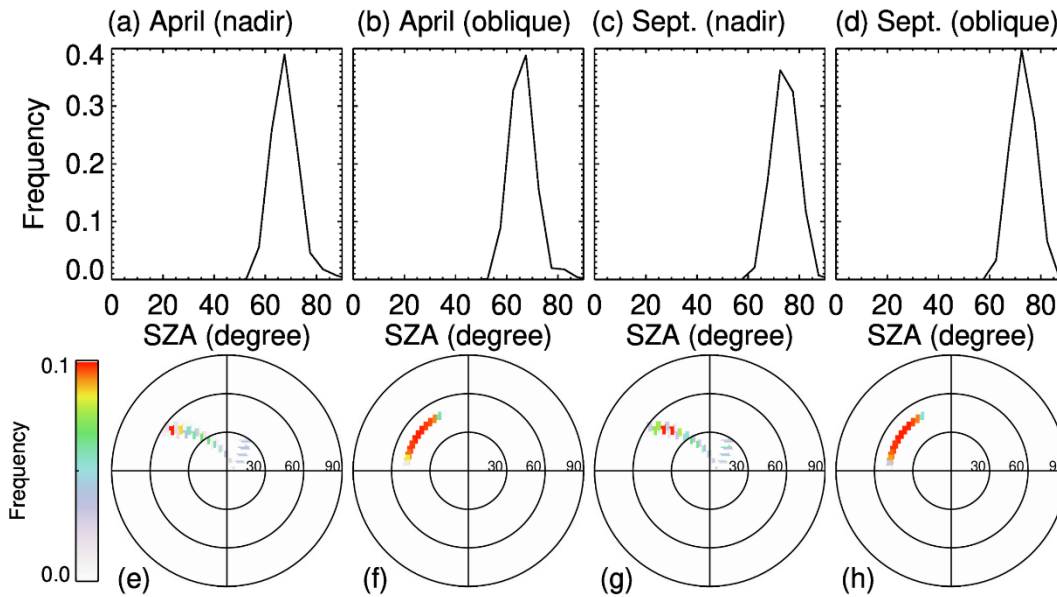
174 **2 Data**

175 **2.1 SLSTR instrument**

176 The satellite data will be used twofold throughout the paper. In the first part, we perform a
 177 statistical analysis of the SLSTR observation/illumination geometries to select realistic settings
 178 for the sensitivity study. In the second part of the companion paper, the satellite measurements

179 will be used as the inputs of the XBAER algorithm to derive the research satellite products of
180 SGS, SPS, and SSA.

181 The SLSTR instrument onboard the European Space Agency (ESA) satellite Sentinel-3 is the
182 successor of the Advanced Along-Track Scanning Radiometer (AATSR) instrument, which is used
183 to maintain continuity with the (A)ATSR series of instruments. SLSTR takes the heritage of AATSR
184 instrument characteristics, especially the dual-viewing observation capabilities and wavelength
185 settings. In order to have a reasonable setting for observation/illumination geometries in the
186 sensitivity study, we perform a statistical analysis of the SLSTR observation geometries (solar
187 zenith angle, SZA, viewing zenith angle, VZA, relative azimuth angle, RAA), similar as Mei et al
188 (2020a). This analysis is essential because 1) it provides a realistic setting of
189 observation/illumination geometries in our sensitivity studies; 2) it helps us to have a complete
190 understanding of the observation/illumination related surface/atmospheric properties. Here the
191 definition of RAA has been harmonized with SCIATRAN (Rozanov et al., 2014), namely, RAA
192 value is equal to 0° under strict glint condition. The statistical analysis has been performed using
193 observations over Greenland during April and September 2017. April and September are reported
194 to be representativeness months of the Arctic (Mei et al., 2020a). Please be noted that these two
195 months are picked up to represent the SLSTR observation characteristic with typical solar
196 illumination angle, the change of underlying surface properties plays no role in such selection. Fig.
197 1 shows the frequency of SLSTR observation geometries. The upper panel shows the SZA with
198 SLSTR nadir and oblique observations for April and September. We can see that the SZA occurs
199 frequently with a value of 70° for selected months. The VZA and RAA for oblique observation mode
200 are typically around 55° and in a range of $[110^\circ, 170^\circ]$, respectively. The observation geometries
201 for nadir observation show relatively large variabilities due to larger swath width compared to
202 oblique (1400 km vs 700 km). Larger SZA can be found especially at the edge of the swath. The
203 VZA and RAA for oblique observation mode are typically in ranges of $[0^\circ, 55^\circ]$ and $[70^\circ, 140^\circ]$,
204 respectively. According to the statistical analysis, a combination of SZA, VZA, RAA of $70^\circ, 30^\circ,$
205 135° for nadir observation and $70^\circ, 55^\circ, 135^\circ$ for oblique observation can be a reasonable setting
206 for the SLSTR observation geometries for the sensitivity study.



208

209 Fig. 1 Upper panel is the histograms of SZA for SLSTR observations: (a) nadir during April;

210 (b) oblique during April, (c) nadir during September; (d) oblique during September. Lower

211 panel is the polar plots of (VZA, RAA) probability for AATSR observations: (e) nadir during

212 April; (f) oblique during April, (g) nadir during September; (h) oblique during September.

213

214 2.2 Laboratory measurements

215 Laboratory measurements of the bidirectional reflectance of snow samples contain important

216 information about the dependence of the angular structure of snow reflection on the lighting

217 geometry, wavelength, and snow physical properties. The comparison of measured and

218 modeled bidirectional reflectance helps to establish the conceptual ideas for the retrieval

219 algorithm. For this comparison, we have selected measurements of fresh and aged snow

220 samples presented by Dumont et al., (2010) and Peltoniemi et al., (2009), respectively.

221 The fresh snow sample, a cylinder of 30 cm diameter and 12 cm height, was taken from

222 new wet snow layer at Col de Porte (Chartreuse, France) at 1300 meter above sea level during

223 January 2008 (Dumont et al., 2010). The sample was stored in a cold room at -10°C for one

224 week to avoid metamorphic effects during the ensuing measurements. To obtain the

225 Bidirectional Reflectance Factor (BRF), the snow sample was illuminated by a monochromatic

226 light source at incidence zenith angle of 60° . The spectral BRF between 500 and 2600 nm was
227 measured at viewing zenith angles of 0° , 30° , 60° , 70° and relative azimuth angles 0° , 45° , 90° ,
228 135° , 180° by a spectrogonio-radiometer developed at the Laboratoire de Planétologie de
229 Grenoble, France, and using a Spectralon® and an infragold® sample as a reference (see
230 Dumont et al., (2010) for further details).

231 The aged snow sample, a cuboid of more than 10 cm height, was taken from an old dry
232 snow layer at Masala, Finland, and brought into a warm laboratory. The spectral BRF between
233 350 and 2500 nm was measured during the aged process by the Finnish geodetic institute field
234 goniospectro-polariphotometer (FIGIFIGO) and using a Labsphere Spectralon 99% white
235 reference plate. For illumination, a 1000 W Oriel Research Quartz tungsten halogen lamp at a
236 zenith angle of 60° was utilized (Peltoniemi et al., 2009). Spectral BRF was obtained at viewing
237 zenith angles up to 70° in 1° resolution and at relative azimuth angles of 0° , 90° , 130° , 160° ,
238 180° , 270° , 310° , and 340° . The first and last measurements were done in the principal plane,
239 indicating minor metamorphism in the snow layer during the measurement.

240

241

242 **3 Dependence of snow reflectance on target parameters**

243 A comprehensive data library (Yang et al., 2013) containing the scattering, absorption, and
244 polarization properties of ice particles in the spectral range from 0.2 to 15 μm was used to
245 calculate radiative transfer through a snow layer (Pohl et al., 2020b). A full set of single-
246 scattering properties is available for nine ice crystal habits presented in Table 1. The maximum
247 dimension of each habit ranges from 2 to 10000 μm in 189 discrete sizes.

248 The optical properties of ice crystals depend on wavelength, ice crystal size, and shape.
249 Maximal dependence of the single-scattering albedo on the particle size is observed in the
250 spectral ranges where ice absorption cannot be neglected. The asymmetry factor depends on
251 the particle size for the whole spectral range. This dependence can be weaker or stronger at a
252 selected wavelength depending on SPS (see Yang et al., (2013) for details).

253 To better illustrate the impact of SGS and SPS on the radiative transfer through a snow
254 layer, we have calculated the reflectance of the snow layer consisting of droxtals, aggregates of

255 8 columns, hollow columns, and plates with crystal surface roughness condition as severely
256 roughened. The simulations of snow reflectance were performed using the radiative transfer
257 package SCIATRAN (Rozanov et al., 2014). The snow layer was defined as a layer directly
258 over a black surface, with snow optical thickness of 500 and a snow geometrical thickness of
259 1m. The snow layer is assumed to be vertically and horizontally homogeneous without any
260 surface roughness and composed of monodisperse ice crystals. The impact of snow impurities
261 and scattering/absorption processes in the atmosphere was neglected at this stage. The
262 reflectance of the snow layer as a function of the effective radius of ice crystal at wavelengths
263 0.55 μm and 1.6 μm is presented in Fig. 2. The calculations were performed for typical SLSTR
264 instrument observation/illumination geometries (see section 2.1), with SZA, VZA, and RAA
265 equal to 70°, 30°, and 135° (scattering angle 129°).

266 There are a couple of criteria we considered for the selection of the optimal wavelengths
267 (0.55 μm and 1.6 μm) in XBAER algorithm, for the purpose of creating a long-term satellite
268 snow properties dataset with good and stable accuracy.

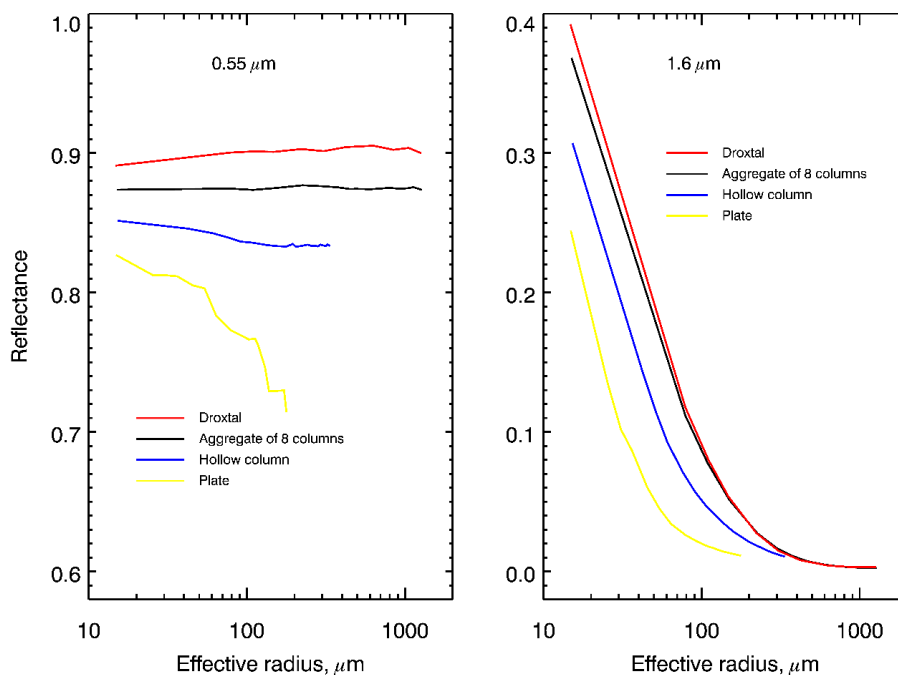
269 ➤ Taking the overlap channels between AATSR and SLSTR because a consistent
270 long-term satellite snow dataset is possible only when the same algorithm can be
271 applied on both AATSR and SLSTR instruments. In particular, the overlap channels
272 between AATSR and SLSTR are 0.55, 0.66, 0.87, 1.6, 3.7, 10.85, and 12 μm .

273 ➤ Picking up wavelengths, for which contribution of thermal emission can be
274 ignored, then 0.55, 0.66, 0.87, and 1.6 μm remain.

275 ➤ Deleting the channel 0.66 μm to avoid the potential impact of O₃ absorption,
276 after that, 0.55, 0.87, and 1.6 μm remain.

277 ➤ Taking into account, that the retrieval algorithm is a two-stage algorithm, namely,
278 first it uses channels with minimum impact of ice crystal shape to retrieve the grain
279 size, and then it selects the shape using channels with minimum impact of grain size.
280 Accounting for that the channel 0.87 μm is impacted by both size and shape, 0.55 and
281 1.6 μm channels were picked up for the retrieval.

282 The right panel of Fig. 2 demonstrates the strong dependence of the snow layer reflectance
 283 at 1.6 μm on the SGS. One can also see that the dependence of snow reflectance on SPS cannot
 284 be neglected. In particular, the same reflectance can be obtained with a combination of different
 285 SGS and SPS. For instance, one can see from the right panel of Fig. 2 that, the reflectance of
 286 the snow layer consisting of droxtals with $\text{SGS}=200 \mu\text{m}$ or of plates with $\text{SGS}=65 \mu\text{m}$ equals
 287 ~ 0.035 in both cases. Thus, assuming different SPSs, the values of retrieved SGS can differ 3
 288 times. The left panel of Fig. 2 demonstrates the dependence of the snow layer reflectance at 0.55
 289 μm on SGS and SPS. It can be seen that the dependence of reflectance on SGS is very weak for
 290 droxtals and aggregate of 8 columns. However, reflectance at 0.55 μm decreases with an
 291 increase of SGS for hollow columns and plates. The weak oscillations for the reflectances at
 292 0.55 μm can be explained by the joint impact of oscillations in the single-scattering albedo and
 293 elements of the scattering matrix presented in the original database. Although the reason for the
 294 oscillation in the database is unclear, it is unlikely due to physical phenomena (Dr. M. Saito ,
 295 personal communication).



296
 297 Fig 2. Reflectance of snow layer at 0.55 μm and 1.6 μm calculated assuming different SPS.
 298 Observation/illumination geometry: SZA, VZA and RAA were set to 70°, 30° and 135°,
 299 respectively.

300 To illustrate this point, the dependence of the phase function at 129° scattering angle on
301 SGS is shown in the left panel of Fig. 3. The phase functions (F11 element of the scattering
302 matrix) were extracted from the original database. According to the left panel of Fig. 3, the
303 dependence of snow surface reflectance at $0.55 \mu\text{m}$ on SGS and SPS is caused mainly by the
304 phase function of ice crystal. Weak oscillations can also be found.

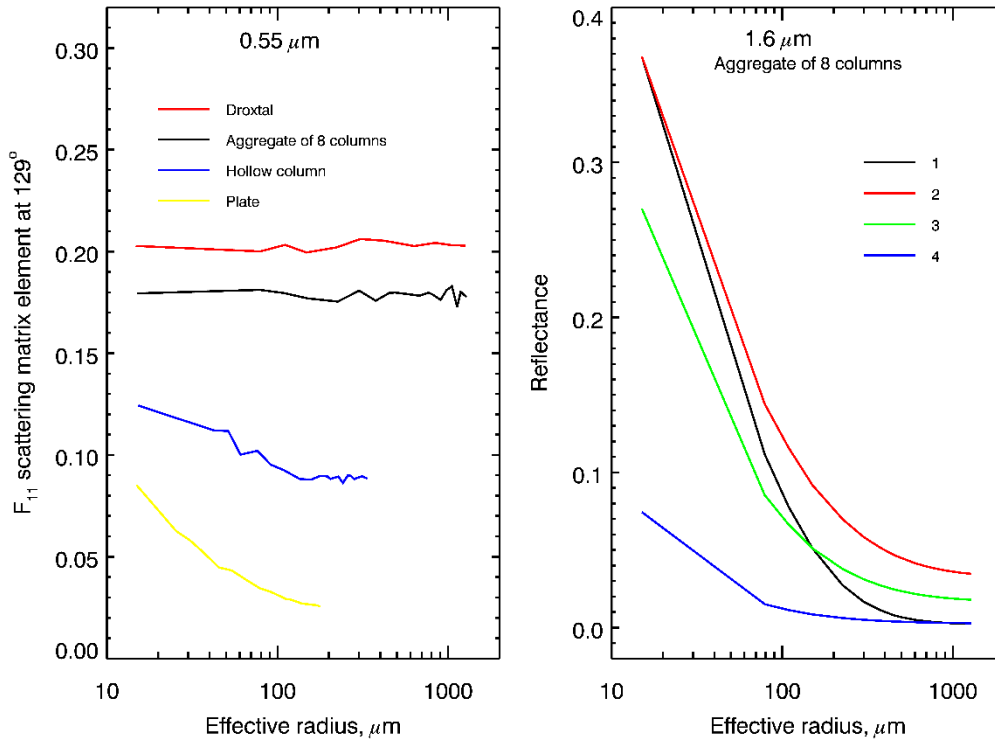
305 The above analysis shows that accurate retrieval of SGS requires adequate information
306 about SPS and accounting for the dependence of the phase function on SGS. To better illustrate
307 the impacts of SGS on ice crystal phase function, we calculated reflectance at $1.6 \mu\text{m}$ with
308 different SGS values. The right panel of Fig. 3 represents the reflectance of the snow layer,
309 consisting of aggregates of 8 columns, calculated accounting for the dependence of the phase
310 function on the effective radius (black line) and assuming constant phase function for three
311 selected effective radii equal to 15, 150, and $1150 \mu\text{m}$ (red, green, and blue lines, respectively).
312 It can be seen that the accurate simulation of snow reflection requires accounting for the
313 dependence of phase function on SGS.

314 The main findings of presented investigations can be formulated as follows:

- 315 ➤ reflectance of a snow layer depends on both SGS and SPS;
- 316 ➤ accurate simulation of snow surface reflectance requires accounting for the dependence of
317 phase function on SGS;
- 318 ➤ spectral channels in the visible spectral range is more sensitive to SPS compared to SGS;
- 319 ➤ spectral channels in the near infrared spectral range is more sensitive to SGS compared to
320 SPS.

321

322



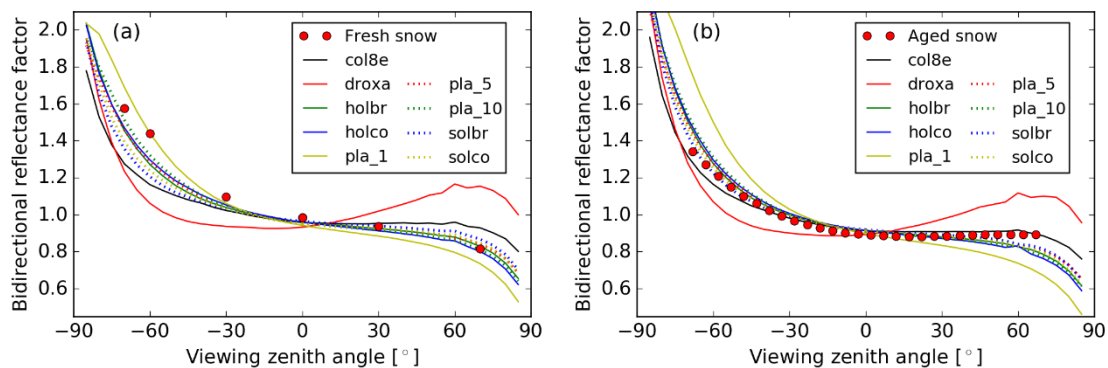
323

324 Fig 3. Left panel: phase function at 0.55 μm for scattering angle of 129°, extracted from the
 325 original database (Yang et al., 2013) as a function of effective radius. Right panel: reflectance
 326 of snow layer at 1.6 μm consisting of aggregate of 8 columns, calculated assuming that: 1:
 327 phase function depends on the effective radius (black line); 2: phase function is constant
 328 corresponding to the effective radius 15μm (red line); 3: same as 2 but for effective radius of
 329 150 μm (green line); 4: same as 2 but for effective radius of 1150 μm (blue line).

330

331 Although the global classification snow crystal, ice crystal, and solid precipitation
 332 particles suggested in Kikuchi et al. (2013) consist of the 121 particle types, we restrict
 333 ourselves, in the retrieval algorithm, with nine shapes of ice crystals, for which optical
 334 characteristics are represented in database (Yang et al., 2013). And these nine shapes have been
 335 proven to be used to reproduce typical wavelength/angular features of snow reflectance in
 336 reality, especially from satellite observations (Räsänen et al, 2015; Pirazzini et al., 2015; Saito
 337 et al., 2019; Schneider et al., 2019; Pohl et al., 2020b). To further illustrate that the selected
 338 dataset is able to reproduce the BRF of different snow types, we compared the simulated and
 339 measured BRF of fresh (Dumont et al., 2010) and aged (Peltoniemi et al., 2009) snow samples.

340 To reproduce the spectral BRF by SCIATRAN, we use the setup described above in this section
 341 and adjust the SGS for each SPS by minimizing the deviation between simulated and measured
 342 reflectance at 1.6 μm . Figure 4 shows the simulated BRF in the principal plane at 0.55 μm of
 343 fresh and aged snow samples, as well as the respective measurements. The BRF is defined as
 344 $\pi I/F$, where I is the reflected radiance and F is the incident irradiance. According to Fig. 4(a),
 345 for fresh snow, plates are the best shape to reproduce the measured BRF in the vicinity of the
 346 forward scattering peak but plates underestimate the BRF at higher viewing zenith angles in the
 347 backscattering region. Here, shapes of hollow bullet rosette, hollow column, aggregate of 10
 348 plates exhibit better potential to simulate the fresh snow layer BRF. In the case of aged snow,
 349 shapes of solid and hollow column, hollow bullet rosette, and aggregate of 5 and 10 plates
 350 provide BRF values in conformity with respective measurements. However, they slightly
 351 underestimate the BRF at high zenith angles in the backscattering region where aggregate of 8
 352 columns can simulate the aged snow BRF better.



353
 354 Fig. 4 The comparison of angle dependence of laboratory-measured and simulated snow
 355 reflectance: (a) fresh snow sample; (b) aged snow sample. Symbols - measurements, lines -
 356 simulations with SCIATRAN assuming different SPS (see legend).

357 The above analysis demonstrates that the selected database of SPS can be used
 358 successfully to reproduce measured BRF of both fresh and aged snow samples. Similar results
 359 were obtained by Pohl et al., (2020b). In this paper, top of atmosphere BRF at 865 nm derived
 360 from POLARization and Directionality of the Earth's Reflectances 3 (POLDER-3) on
 361 Polarization & Anisotropy of Reflectances for Atmospheric Sciences coupled with
 362 Observations from a Lidar (PARASOL) measurements over a pure snow surface in Greenland

363 (70.5° N, 47.3° W) on 6 July 2008 were compared with the SCIATRAN simulations, using
364 droxtals, solid bullet rosettes, and solid columns.

365 According to the above analysis, we can formulate the general algorithm to retrieve SGS
366 and SPS from satellite observations. Satellite provides the wavelength-dependent TOA
367 reflectance, for a given SGS and SPS pair, the minimization between satellite observed TOA
368 reflectance and theoretical simulation is performed. The optimal SGS and SPS are obtained
369 when the difference between observations and simulations reaches the predefined criteria. The
370 SSA is then calculated by the retrieved SGS and SPS.

371

372 **4 XBAER Algorithm**

373 The retrieval algorithm consists of three stages. The first stage includes the estimation of
374 SGS using the effective Lambertian surface albedo after atmospheric correction for selected
375 observation geometries and wavelengths. This step is performed based on the path radiance
376 representation (Mei et al., 2017), in which the TOA reflectance can be described by the
377 contribution from the atmosphere and the interaction between atmosphere and surface. The
378 inverse to derive the surface reflectance from the satellite observed TOA reflectance is called
379 the atmospheric correction. And due to certain assumptions in the path radiance
380 representation, the derived surface reflectance is equivalent to the effective Lambertian
381 surface albedo. The estimation of SGS is obtained solving the following minimization
382 problem with respect to the effective radius, r , of snow crystals:

$$383 \quad \|\mathbf{A}_e - \mathbf{R}_s(r)\|^2 \rightarrow \min. \quad (1)$$

384 Here, \mathbf{A}_e and $\mathbf{R}_s(r)$ are two vectors which components are the effective Lambertian
385 surface albedo and the simulated snow reflectance, respectively. The dimension of these
386 vectors is the number of wavelengths times the number of viewing directions.

387 The simulation of snow reflectance (components of vectors $\mathbf{R}_s(r)$) was performed using
388 the radiative transfer package SCIATRAN (Rozanov et al., 2014) as described in Section 3.

389 The optical properties of nine SPSs, listed in Table 1, were used for radiative transfer
390 calculations.

391 The minimization problem formulated by Eq. (1) was solved separately for each SPS
392 using Brent's method (Brent, 1973). The solution of the minimization problem for each
393 crystal habit is characterized by the following residual:

$$394 \quad \Delta_i = \|A_e - R_s(r_i^*)\|^2, i = 1, 2, \dots, 9, \quad (2)$$

395 where r_i^* is the solution of minimization problem given by Eq. (1) for i^{th} shape of the ice
396 crystal particle.

397 The second stage is the selection of such i (SPS) for which Δ_i is minimal. This
398 completes the retrieval process and enables the optimal SGS and SPS to be obtained.

399 The third stage is to calculate SSA for the retrieved SGS and SPS. To this end, let us
400 rewrite the SSA introduced above in the following equivalent form:

$$401 \quad \text{SSA} = 3/\rho r \cdot (A_t/4A_p), \quad (3)$$

402 where r is the effective radius. According to Cauchy's surface area formula (Cauchy, 1841;
403 Tsukerman and Veomett, 2016), the average area of the projections of a convex body is
404 equal to the surface area of the body, up to a multiplicative constant. In our case, this results
405 in $A_t = 4A_p$ and SSA for convex particles such as droxtals, solid columns, and plates are
406 equal to $3/\rho r$. In the case of non-convex particles, the calculation of SSA requires the
407 information about total area A_t . Although the database given by Yang et al. (2013) does not
408 contain information about A_t , the total area of non-convex particles can be calculated
409 employing geometric parameters of ice crystal habits presented in Table 1 of Yang et al.
410 (2013). Here we take a typical SPS, aggregate of 8 columns, as an example, to show the
411 difference between SSA calculated assuming convex and non-convex particle.

412 According to M. Saito (private communication), the parameters L and a of the
413 aggregate of 8 columns (see Fig. 3 in Yang et al (2013) for details) can be obtained by

414 scaling with respect to the maximum dimension, D . To find these values for different
 415 maximal dimensions, we calculate at first the volume of aggregate of 8 columns
 416 corresponding to parameters a and L on a relative scale as given in Table 1 of Yang et al
 417 (2013).

$$418 \quad V_r = \frac{3\sqrt{3}}{2} \sum_{i=1}^8 a_i^2 L_i. \quad (4)$$

419 Using the database of Yang et al (2013), one can obtained the maximal dimension, D_r ,
 420 corresponding to the volume, V_r . Introducing the scaling factor, $C_k = D_k/D_r$, we have semi-
 421 width and length for the aggregate with the maximal dimension D_k :

$$422 \quad a_{i,k} = a_i C_k, \quad L_{i,k} = L_i C_k. \quad (5)$$

423 The total surface of the aggregate on relative scale is given by

$$424 \quad S_r = 3 \sum_{i=1}^8 (\sqrt{3} a_i^2 + 2 a_i L_i). \quad (6)$$

425 Accounting for Eq (5), we have

$$426 \quad S = C_k^2 S_r. \quad (7)$$

427 Having obtained the total area, one can calculate SSA as the total surface area of a
 428 material per unit of mass:

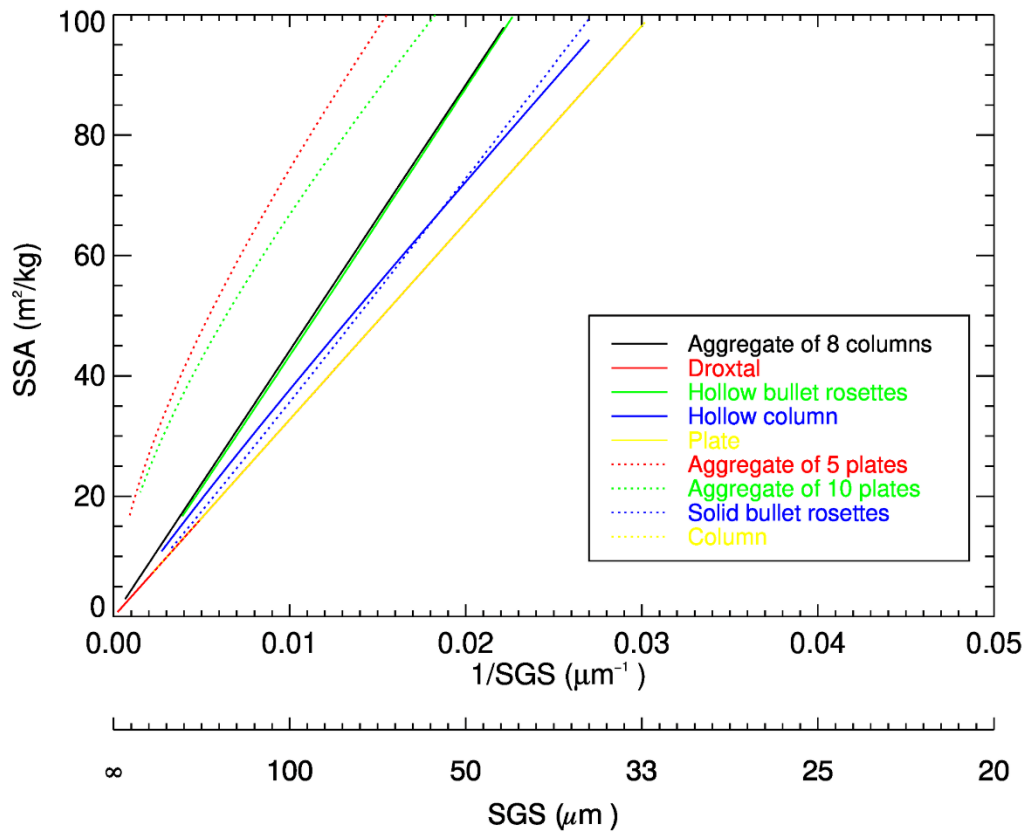
$$429 \quad SSA = \frac{S}{\rho V} = \frac{S_r}{\rho C_k V_r}. \quad (8)$$

430 Comparing SSA of convex particle equal to $3/\rho r$ with result given by Eq. (8), one can
 431 easily notice the difference of SSA calculated from different SPS using the same SGS. The
 432 details of such calculations for other non-convex ice crystal habits are given in the Appendix.

433 The relationship between SSA and SGS for different SPS is presented in Fig. 5. According
434 to Fig. 5, an almost inverse linear relationship between SSA and SGS can be found. The lines,
435 representing droxtal, plate, and column, are overlapped, indicating the same SSA for convex
436 particles. For other SPSs with the same SGS, SSA is larger compared to convex faceted
437 particles. SSA is restricted in the range of 0-100 m²/kg in this investigation (Picard et al.,
438 2009). For example, for SGS=100μm, the SSA is 32.7 m²/kg for convex faceted particles,
439 whereas SSAs for aggregate of 8 columns, hollow bullet rosettes, hollow column, aggregate of
440 5 plates, aggregate of 10 plates, and solid bullet rosettes are 44.2, 43.4, 37.7, 74.4, 66.8 and
441 35.6 m²/kg, respectively. The relative differences range from 9%-128%, depending on the SPS.
442 Taking into account the definition of SSA, one can derive the following relationship between
443 SSA convex and non-convex particles: $SSA_{nc} = SSA_c \cdot (A_i/4A_p)$, where subscript c and nc
444 denotes convex and non-convex particle, respectively. The obtained results reveal that for all
445 non-convex ice crystals under consideration $A_i/4A_p > 1$ and the ratio $A_i/4A_p$ weakly depends
446 on the SGS.

447

448



449

450 Fig 5. Relationship between SGS and SSA for different SPS. For a better illustration, the
 451 realistic range of specific surface area is limited to 100 m²/kg.

452

453 **5 Impact of model parameters uncertainty**

454 The accuracy of any retrieval algorithm depends not only on measurement errors but also on
 455 the uncertainty of parameters which cannot be retrieved. In our case, such parameters are ice
 456 crystal roughness, aerosol, and cloud contamination. The impacts of these factors on XBAER-
 457 derived SGS and SPS have been investigated and will be discussed in this section. The TOA
 458 reflectances at selected channels (0.55 and 1.6 μm) and observation directions for SZA, VZA,
 459 and RAA of 70°, 30°, and 135° for nadir 70°, 55°, and 135° for oblique, respectively, were
 460 calculated using radiative transfer model SCIATRAN. The details of each scenario will be
 461 presented in the corresponding sub-section below.

462

463

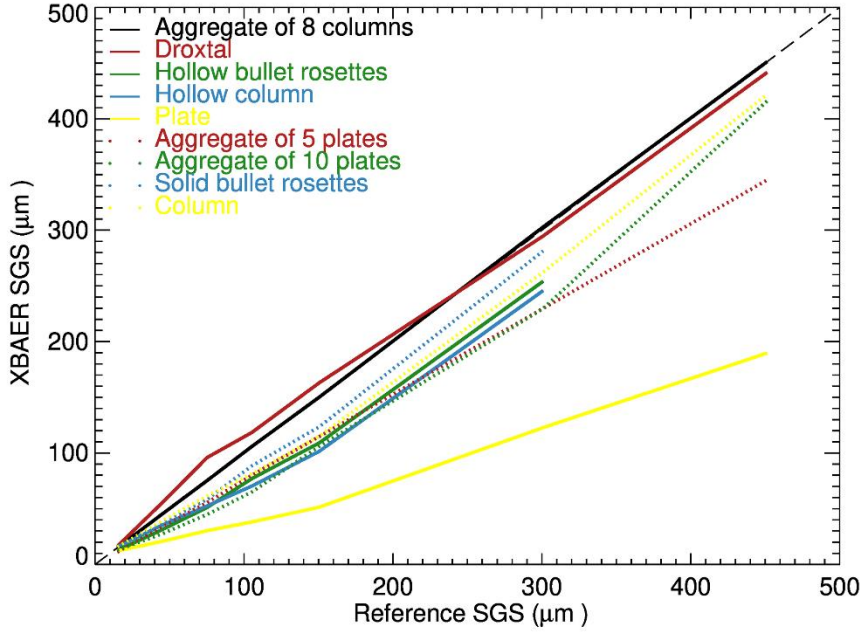
464 **5.1 Impact of snow particle shape**

465 Since the first stage of the XBAER algorithm is to estimate the SGS assuming a given SPS, it
466 is reasonable to investigate the impact of SPS on the retrieval of SGS. The TOA reflectances
467 of a snow layer at 0.55 and 1.6 μm with above-given observation geometries were calculated
468 using the following settings for snow layer and atmospheric parameters:

- 469 ➤ **Snow Layer:** consists of ice crystals with SPS set to be severely roughened aggregate of
470 8 columns and maximal dimensions [100, 300, 500, 700, 1000, 2000, 3000, 5000] μm ,
471 which corresponds to SGS [15, 45.1, 75.2, 105.3, 150.4, 300.8, 451.3, 752.1] μm .
- 472 ➤ **Atmosphere:** excluded

473

474 The simulated snow reflectances were used as components of vector \mathbf{A}_e in Eq (1). Nine
475 SPSs from database presented in Yang et al. (2013) are used sequentially in the retrieval process.
476 The atmospheric correction is not performed because the atmosphere is excluded in the forward
477 simulations. This enables avoiding additional errors caused by the atmospheric correction and
478 estimates the pure effect of SPS on the retrieval results. Fig.6 shows the impact of the SPS on
479 SGS retrieval. Different colors and line styles indicate different ice crystals used in the retrieval
480 process. The black solid line represents the retrieved SGS assuming SPS in the retrieval process
481 is the same as in forward simulations. This line agrees well with the 1:1 line, indicating that the
482 retrieval algorithm has been implemented technically correct. According to Fig.6, one can see
483 both underestimation and overestimation of SGS depending on the SPS used in retrieval.
484 However, in most cases, an incorrect SPS leads to an underestimation of SGS. In particular, the
485 maximal effect can be seen when ice crystals of plate shape, rather than the correct aggregate
486 of 8 columns, is used (yellow solid line). This result can be easily explained coming back to the
487 right panel of Fig. 2. Indeed, one can see that the same reflectance of the snow layer can be
488 obtained using the plate shape, instead of an aggregate of 8 columns, with significantly smaller
489 SGS. These results reveal that the SPS is an important parameter affecting the accuracy of
490 retrieved SGS.



491

492

Fig 6. Impact of SPS on the retrieval of SGS.

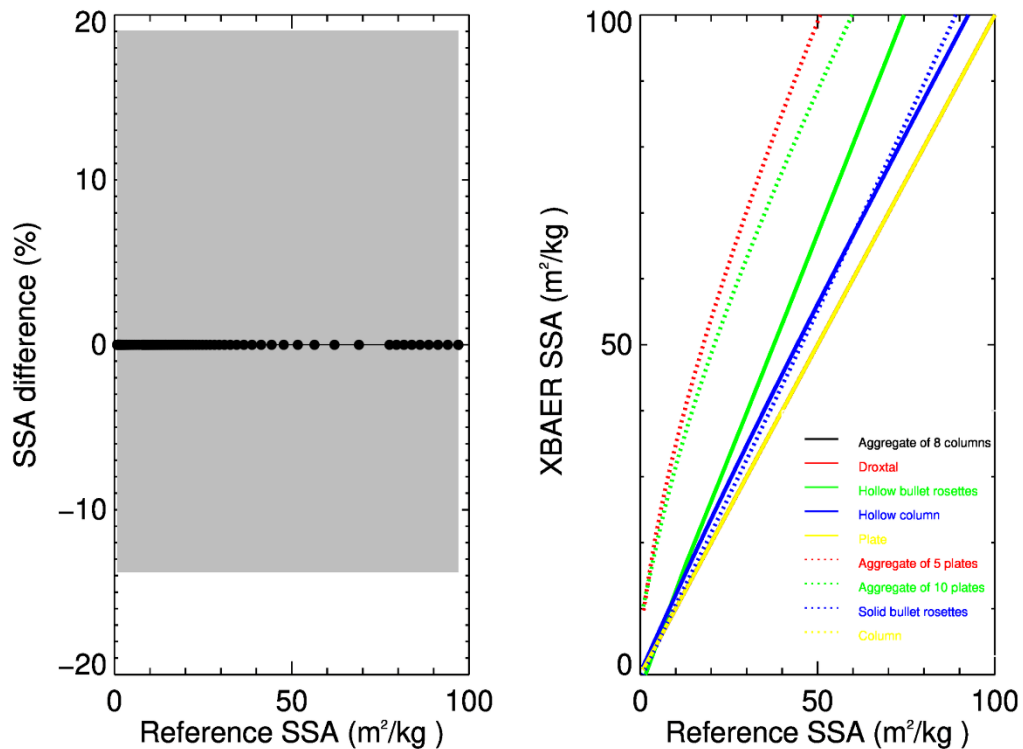
493

494 5.2 Impact of SGS/SPS on SSA

495 Since the SSA is obtained from the retrieved SGS and SPS, an understanding of how the
 496 error of SGS and/or SPS propagates to the SSA will provide helpful information to understand
 497 the retrieved SSA. Fig. 7 shows the impact of SGS (left) and SPS (right) on XBAER retrieved
 498 SSA. The relative error of SGS, $\epsilon_r = (r - r')/r$, is propagated to the relative error of SSA as ϵ_{SSA}
 499 $= 1 - 1/(1 - \epsilon_r)$, and it is independent of reference SSA. The left panel of Fig. 7 depicts ϵ_{SSA}
 500 corresponding to ± 0.16 of ϵ_r . One can see that this results in 19% and -13.8% of SSA relative
 501 errors, which are presented as the upper and lower error boundaries in the left panel of Fig. 7.
 502 The systematical error of $\pm 16\%$ for SGS was obtained as the maximal relative difference
 503 between XBAER retrieved SGS and both *in-situ* and aircraft measured SGS (as presented in
 504 the companion paper). This represents the worst case of SGS error propagation into SSA.

505 The impact of SPS on SSA is demonstrated in the right panel of Fig. 7. As a reference
 506 shape, we have selected in this case the plate, which provides the same SSA as other convex
 507 particles. One can see that the SSA of non-convex particles overestimates the SSA of convex
 508 particles, which is in line with the results presented in Section 4. For instance, for the same

509 SGS, the SSA for aggregate 8 columns (non-convex particle) is about 3 times larger than that
 510 for doxtal (convex particle). Since the assumption of the sphere (convex particle) is used to
 511 measure SSA in-field measures (Gallet et al., 2009; Personal communication with Dr. Nick
 512 Rutter), such as observations from SnowEx, the retrieval results of SSA from XBAER will be
 513 systematically larger than field measurements in the case of non-convex particles even if the
 514 retrieved and measured SGS are similar. However, a detailed discussion with respect to
 515 uncertainty in the campaign-based measurement is out of the scope of this manuscript.



516
 517 Fig 7. Impact of SGS and SPS on the retrieval of SSA. Left panel (SGS errors): the black line
 518 with dots indicate the 0 difference for accurate SGS for aggregate 8 column, the grey area
 519 indicate the relative error of SSA introduced by 16% error of SGS; Right panel (SPS selection):
 520 different color/line styles indicate different SPS used in the calculation of SSA while the true
 521 SPS is set to be „ plate“ or other convex particles.

522

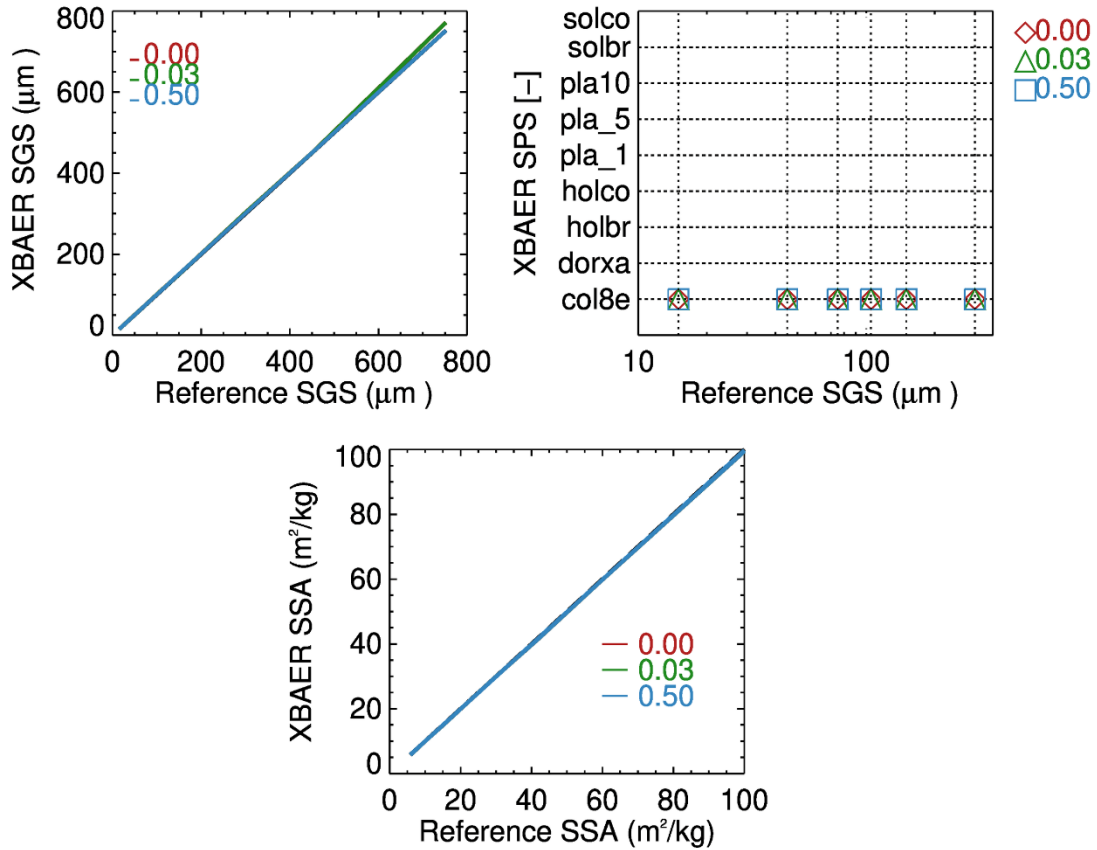
523

524 **5.3 Impact of ice crystals surface roughness**

525 Although surface roughness of ice crystal is not so severe for snow compared to ice
526 cloud due to basic thermodynamics (Colbeck, 1980, 1983), the Ice Crystal Surface
527 Roughness (ICSR), indicating ice crystal surface texture, may still be important for the retrieval
528 of snow properties from optical sensors such as SLSTR. The ICSR has been used as a new
529 variable in model simulation (Järvinen et al., 2018). Retrieval algorithms of ice cloud
530 parameters frequently based on the assumption that the ice crystal surface is smooth
531 (Kokhanovsky et al., 2019). This assumption can yet introduce large uncertainty in the ice cloud
532 retrieval parameters and, as a consequence, lead to misunderstanding the impacts of ice cloud
533 on global climate change (Järvinen et al., 2018). However, this issue has not yet been discussed
534 for snow. In general, ice crystal surfaces are rougher in clouds than in snow layers due to
535 metamorphism processes (Colbeck, 1980, 1983; Ulanowski et al., 2014). The investigation of
536 the impact of ICSR on retrieval of snow properties provides valuable information to understand
537 the XBAER algorithm. The ICSR according to Yang et al., (2013) is defined similarly as
538 suggested by Cox and Munk (1954) for the roughness of the sea surface. A parameter σ
539 describes the degree of ICSR. The σ values 0, 0.03, and 0.5 are for three surface roughness
540 conditions: smooth, moderate roughness, and severe roughness. And only the above three
541 values are available in the Yang database. The snow layer reflectances were used as components
542 of the vector \mathbf{A}_e in Eq. (1) in the same way as in Section 5.1.

543 Fig. 8 shows the impact of ICRS on the retrieved SGS, SPS, and SSA. The impact of ICRS
544 on SGS and SSA are relatively small for SGS smaller than $\sim 300 \mu\text{m}$. Ignoring the impact of
545 roughness leads, in general, to a slight overestimation on SGS and an underestimation of SSA.
546 The absolute errors of SGS and SSA introduced by ICRS range from 0.3% - 3%, depending on
547 SGS. Due to the inverse almost linear relationship between SSA and SGS, as presented in Fig.
548 5, for the same SPS, an overestimation of SGS leads to an underestimation of SSA. The slight
549 overestimation can be found if less ICRS is taken into account in retrieval because the snow
550 reflectance with the same SGS and SPS for ICRS = 0.5 is larger than for ICRS = 0.03 due to
551 lower asymmetry factor of ice crystal with more roughened surface roughness, thus the same
552 surface reflectance observed by satellite requires larger SGS for the case with ICRS = 0.03 used

553 in retrieval in contrast to ICRS = 0.5 used in the forward simulation. However, as can be seen
 554 from the right panel of Fig.8, the XBAER algorithm still retrieves the correct SPS ignoring the
 555 impact of roughness.



556
 557 Fig 8. Impact of Ice Crystal Surface Roughness (ICRS) on the retrieval of SGS (upper left)
 558 SPS (upper right) and SSA (lower). Different colors indicate different ICSR used in the
 559 retrieval.

560

561 **5.4 Impact of aerosol contamination**

562 The impact of aerosol on the retrieval of snow properties using passive remote sensing can be
 563 important because there is limited aerosol information over the cryosphere (Mei et al., 2013a;
 564 Mei et al., 2013b; Mei et al., 2020a; Tomis et al., 2015) to perform an accurate atmospheric
 565 correction. The use of MERRA simulated AOT, although with good data quality, will still
 566 introduce potential aerosol contamination in the XBAER-derived snow properties. The impact
 567 of aerosol on snow properties retrieval is much smaller over Arctic regions compared to middle-

568 low latitude (e.g. Canadian Arctic, Tibetan Plateau) due to large absolute uncertainty in the
569 MERRA simulated aerosol over middle-low latitude in wintertime. A detailed comparison of
570 how possible aerosol contamination may affect the retrieved snow properties will be included
571 in the companion paper (Mei et al., 2020c). In the companion paper, the comparison between
572 satellite-derived and campaign-measured snow properties all over the world will be included.
573 In order to have a better understanding of aerosol contamination on snow properties retrieval,
574 the TOA reflectances were calculated at 0.55 and 1.6 μm with above-given observation
575 geometries using the following settings:

576 ➤ **Snow Layer:** Same as in section 5.1;

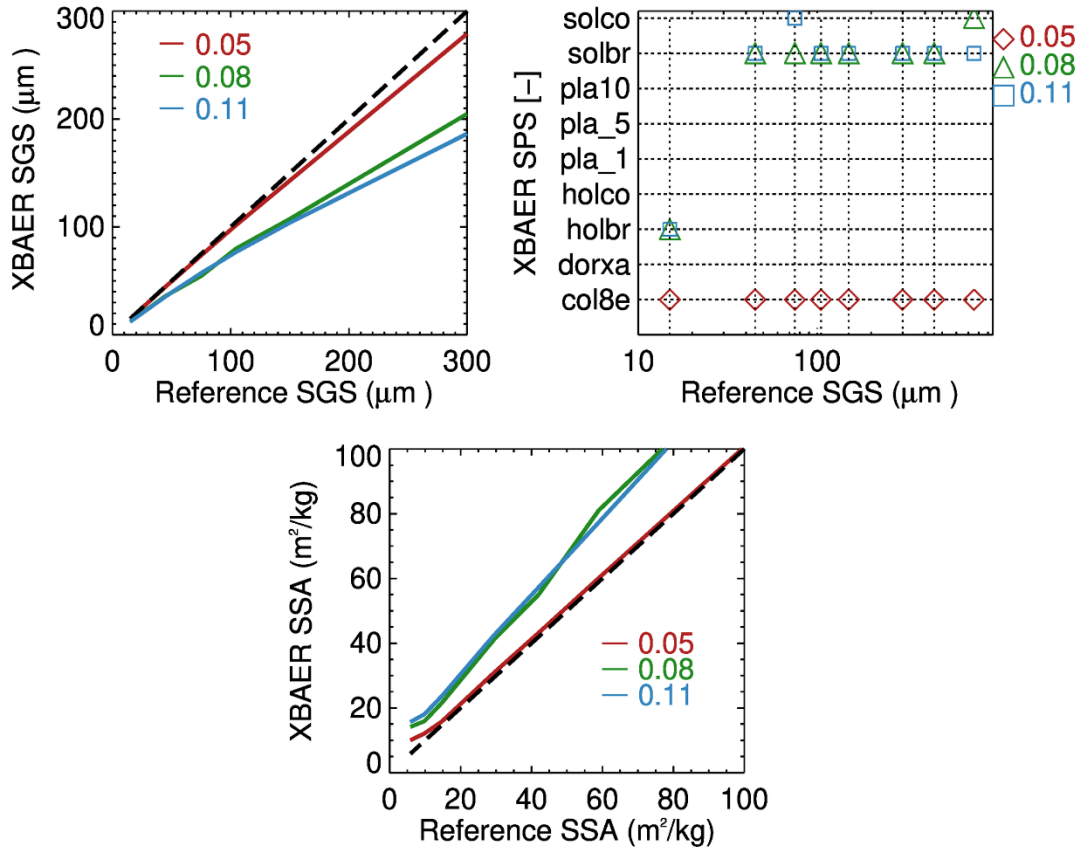
577 ➤ **Atmosphere:**

- 578 ● Aerosol type is set to be weakly absorbing (Mei et al., 2020b) with AOTs [0.05, 0.08, 0.11].
579 Other atmospheric parameters are set according to Bremen 2D Chemical transport model
580 (B2D CTM) for April at 75° N (Sinnhuber et al., 2009). It is worth to notice this three AOT
581 values represent background, average, and pollution conditions in the Arctic as suggested
582 by Mei et al (2020a; 2020b).

583 Fig.9 shows the impact of aerosol contamination on the SGS (upper left), SPS (upper right),
584 and SSA (lower) retrieval. These results are obtained by introducing 50% error in AOT at the
585 step of atmospheric correction and can be considered as the worst case for impact of aerosol
586 contamination on retrieved SGS, SPS, and SSA. The surface reflectances estimated after
587 employing the atmospheric correction were used as components of the vector \mathbf{A}_e in Eq. (1). One
588 can see that aerosol introduces systematic underestimation of retrieved SGS for the given
589 scenarios and the magnitude of underestimation increase with the increase of AOT. For a typical
590 background Arctic aerosol condition, with AOT=0.05, aerosol contamination introduces errors
591 in SGS of less than 3% for $\text{SGS} \leq 150 \mu\text{m}$, and less than 7% for $150 \leq \text{SGS} < 300 \mu\text{m}$. The
592 maximal errors introduced by the aerosol contamination increase to 30% and 37% in the case
593 of average and pollution conditions for AOT=0.08 and 0.11, respectively. Please be noted that
594 the AOT values in the Arctic can be even smaller than 0.05, for instance, AOT over Greenland.
595 Thus, the analysis with respect to aerosol contamination is the worst case for a typical Arctic
596 condition.

597 For the case of $AOT = 0.05$, SPSs have been correctly retrieved for all SGS values,
598 indicating that under a typical Arctic clean condition, the impact of aerosol is not so large to
599 disturb SPS retrieval. In order to demonstrate the two stages retrieval process and illustrate the
600 impact of aerosol, let us focus on Fig. 10. To facilitate the presentation, we consider the
601 measurement of reflectance at $1.6 \mu\text{m}$ for a single observation direction (30°) and at $0.55 \mu\text{m}$
602 for the difference of reflectance at two observation angles (30° and 55°). This enables avoiding
603 the minimization process given by Eq. (1) and represents the retrieval process in the simple
604 graphic form. The left panel of Fig. 10 depicts the determination of an effective radius for each
605 ice crystal form, assuming the correct shape is aggregate of 8 columns with an effective radius
606 $105.4 \mu\text{m}$. Solid and dotted lines are surface reflectance of the snow layer consisting of ice
607 crystals with different forms and the dashed line is the measured reflectance after the
608 atmospheric correction. The obtained SGSs are in the range $40 - 120 \mu\text{m}$, depending on the
609 selected SPS, and presented in Fig. 10 by solid and dotted vertical lines. In the case of correct
610 SPS selection (aggregate of 8 columns) the retrieved SGS is $\sim 110 \mu\text{m}$. The right panel of Fig.
611 10 shows the second stage of the retrieval process, namely, the selection of such SPS for which
612 the difference between measured (dashed line) and simulated value (solid black line) is minimal.
613 In the case under consideration the correct shape is selected with an effective radius $\sim 110 \mu\text{m}$.

614 For larger AOT conditions, an inaccurate selection of SPS occurs for all SGS cases,
615 indicating the remaining aerosol information is large enough to decouple the aerosol
616 contribution from the snow surface characteristic. Thus, a quality flag of SPS, associated with
617 AOT, should be introduced in the retrieval of real satellite data. It is interesting to see that “solid
618 bullet rosettes” is the preferable SPS for very strong aerosol contamination cases. This is due
619 to similar scattering properties (shape) of ice crystal and weakly absorbing aerosol, defined in
620 forward simulation. The impact of aerosol contamination, for typical Arctic conditions,
621 introduces less than 5% error in SSA. However, for large aerosol contamination, the around 30%
622 underestimation in SGS linearly introduced about 25% overestimation in SSA, which agrees
623 with the analysis as presented in Fig.7.



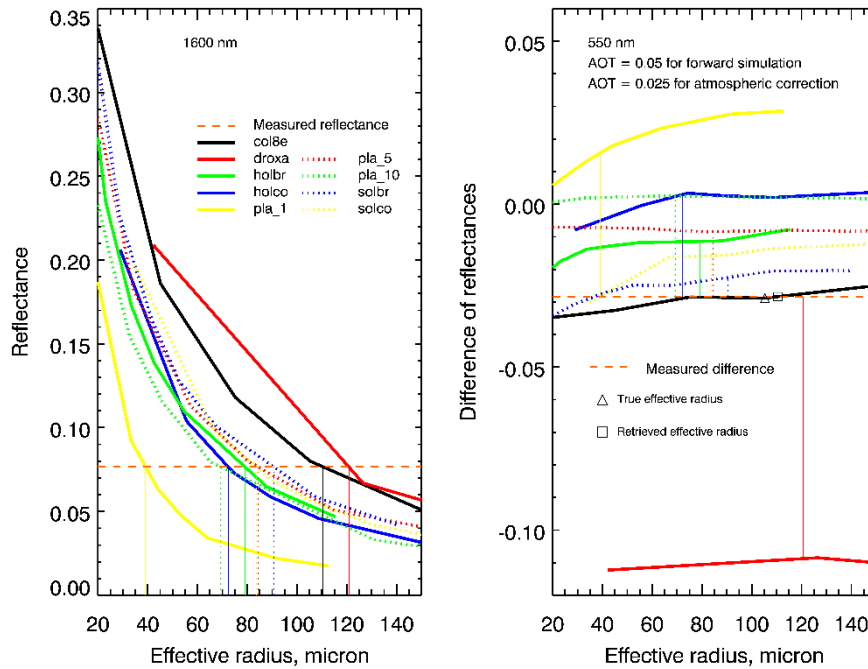
624

625 Fig 9. Impact of aerosol contamination on the retrieval of SGS (upper left) SPS (upper right)

626 and SSA (lower). Different colors indicate different AOT used in forward simulations. No

627 atmospheric correction is performed in the retrieval, black dash line is the 1:1 line.

628



629

630 Fig 10 Schematic representation two stages of the retrieval process. Left panel: determination
 631 of effective radius for each ice crystal form. Right panel: selection of optimal SGS, SPS pair.

632

633 6 Impact of cloud contamination

634 Any cloud screening method, especially over the cryosphere, may introduce cloud
 635 contamination for the retrieval of atmospheric and surface properties (Chen et al., 2014; Mei et
 636 al., 2017; Jafariserajehlou et al., 2019). Understanding of the cloud contamination will
 637 provide valuable information to interpret the retrieval results using the SLSTR instrument. To
 638 investigate the impact of cloud contamination, the following settings were used to perform the
 639 simulations of TOA reflectance:

640 ➤ **Snow Layer:** Same as section 5.1;

641 ➤ **Atmosphere:** Aerosol free atmosphere with other parameters as in section 5.4.
 642 Additionally, vertically homogeneous ice cloud consisting of aggregate of 8 columns with
 643 effective radius of 45 μm and optical thickness [0.1, 0.5, 1.0, 5] is set to be at position of
 644 [5 km, 6 km].

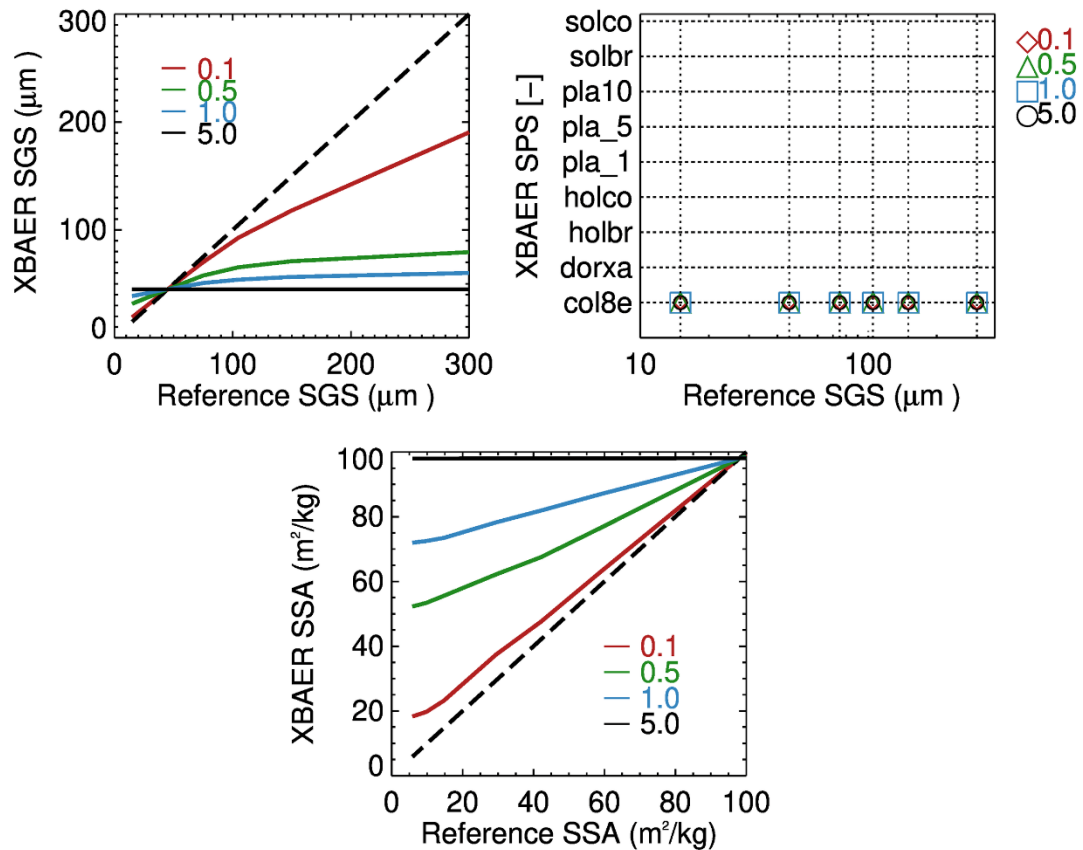
645 Fig. 11 shows the impact of cloud contamination on XBAER retrieved SGS (upper left),
 646 SPS (upper right), and SSA (lower). The size of ice crystals in ice clouds is typically smaller
 647 than snow grain size (Kikuchi et al., 2013). Our statistical analysis of ice crystal effective radius

648 over Greenland shows an average value in the range of 30-50 μm , which is consistent with
649 previous publications (King et al., 2013; Platnick et al., 2017). According to Fig.11, an
650 overestimation of SGS can be found for SGS less than 45 μm (cloud effective radius) and an
651 underestimation of SGS for SGS larger than 45 μm . The magnitude of
652 overestimation/underestimation increases with the increase of Cloud Optical Thickness (COT).
653 XBAER derived SGS becomes saturated for COT larger than 0.5. Due to limited photon
654 penetration depth for optically thicker clouds (e.g., COT = 5), the XBAER algorithm retrieves
655 the effective radius of ice crystal in the cloud. This demonstrates that theoretically, the XBAER
656 algorithm can retrieve an ice cloud effective radius without a pre-processing of cloud screening.
657 And this can be further used as post-processing to avoid cloud contamination.

658

659 The impact of the cloud on the retrieval of SPS is similar to the impact of aerosol
660 considered above. In short, the cloud plays a larger role for larger SPS (darker TOA) and this
661 impact increases with the increase of COT. However, cloud with large COT can be much easier
662 detected and excluded by the cloud screening algorithm (e.g for the cases with COT > 0.5).
663 SPSs are correctly picked up due to the same SPS used for both the snow layer and the cloud
664 layer. Similar to the impact of aerosol, the underestimation of SGS introduced by the cloud
665 leads to an overestimation of SSA (Fig. 11 (lower panel)). The increase of COT results in
666 saturation of the ice cloud SSA, with a value of 100 m^2/kg in the case of aggregate of 8 columns.

667



668

669 Fig 11. Impact of cloud contamination on the retrieval of SGS (upper left) SPS (upper right)
 670 and SSA (lower). Different colors indicate different COTs in forward simulations, black dash
 671 line is the 1:1 line.

672

673 7 Impact of other factors occurring in reality

674 The above theoretical investigations include all possible important factors affecting the
 675 accuracy XBAER algorithm. However, when applying XBAER algorithm to the SLSTR
 676 instrument for real scenarios, two additional factors need to be considered as well. One is the
 677 impact of the instrument spectral response function (SRF), the other one is the
 678 representativeness of the snow scenario for reality.

679 7.1 Impact of instrument spectral response function

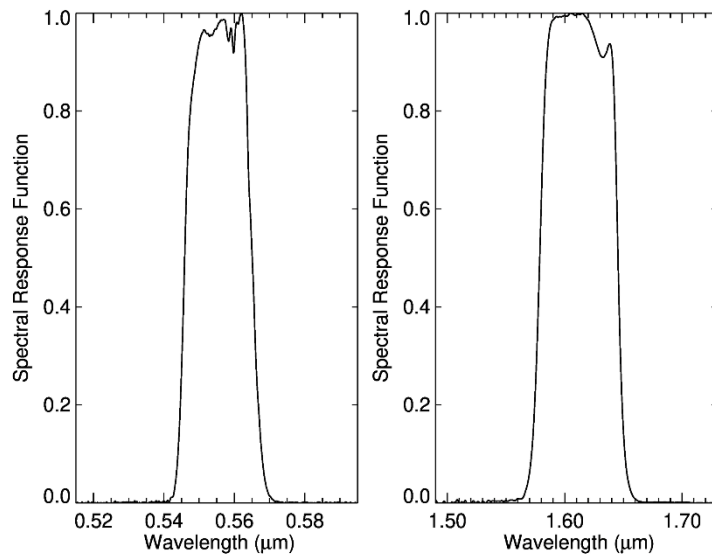
680

681 ➤ **Snow Layer:** Same as section 5.1;

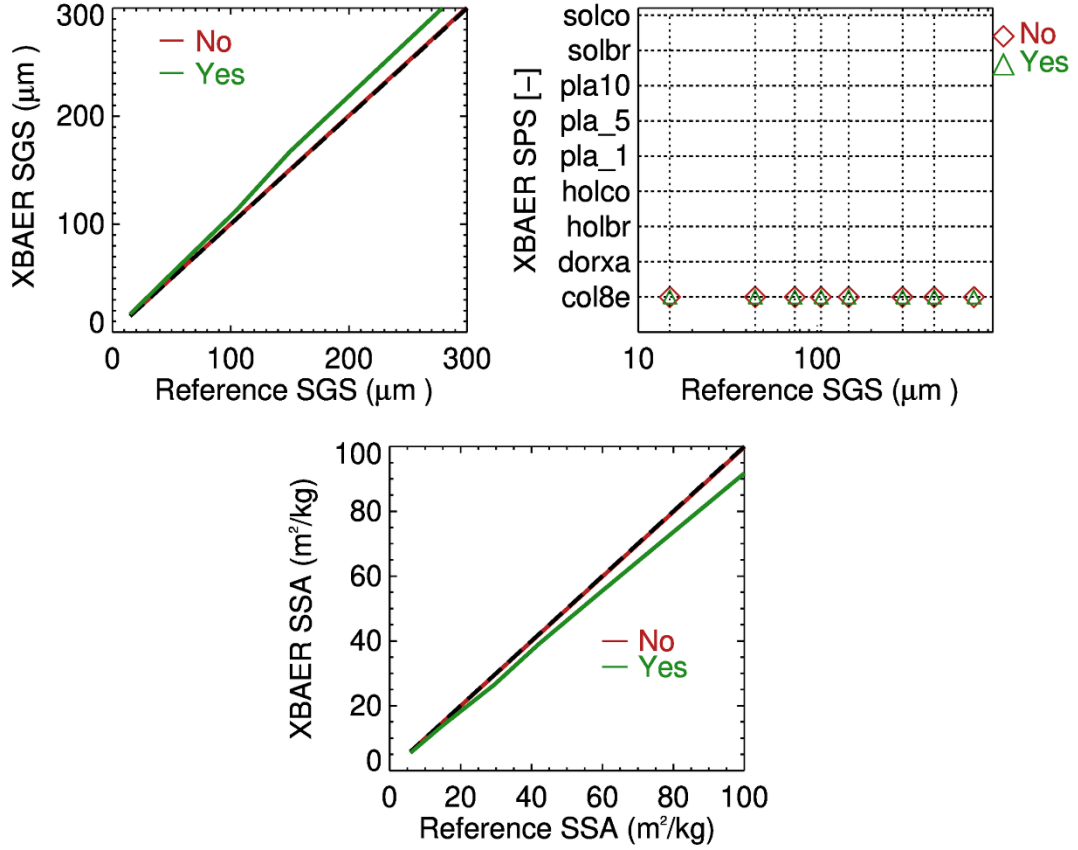
682 ➤ **Atmosphere:** Aerosol free atmosphere with other parameters as in section 5.4.

683

684 The forward simulations are performed with and without the impact of Spectral Response
685 Function (SRF). The SRFs for SLSTR at 0.55 and 1.6 μm are shown in Fig. 12. The retrieval
686 is then performed ignoring SRF. Fig. 13 shows the impact of SRF on the retrieval of SGS, SPS,
687 and SSA. For forward simulations without taking SRF into account (labeled as No in Fig. 13),
688 SGS, SPS, and SSA are well received as expected. And it agrees with Fig. 6. However, ignoring
689 the impact of SRF introduces about 7% uncertainties in the simulated surface reflectance and
690 this causes about 5-7% error in both SGS (overestimation) and SSA (underestimation). Taking
691 SRF into account leads to a smaller surface reflectance at 1.6 μm due to potential gas absorption
692 at this wavelength, thus introduces an overestimation for SGS. However, due to a significantly
693 smaller impact at 0.55 μm , the SRF does not play a significant role in the retrieval of SPS.



694
695 Fig. 12 Spectral response function of 0.55 (left) and 1.6 (right) μm of the SLSTR
696 instrument
697



698

699 Fig. 13 Impact of SRF on the retrieval of SGS (upper left) SPS (upper right) and SSA (lower).

700 Different colors indicate retrieval results without (No) and with (Yes) SRF in forward
 701 simulations, black dash line is the 1:1 line.

702

703

704 7.2 Impact of snow inhomogeneities

705 In this section, a realistic model of snow layer is represented by vertically inhomogeneous,
 706 polydisperse ice crystals habit mixture. Following Saito et al (2019), the gamma distribution
 707 with respect to the maximal dimension will be used to describe polydisperse properties:

$$708 \quad n(D) = NG(D), \quad (9)$$

709 Here, N is the number of ice particles per unit volume, G(D) is the gamma distribution function,
 710 i.e.,

$$711 \quad G(D) = C(D/v)^{k-1} e^{-D/v}, \quad (10)$$

712 where k and v are the shape and scale parameters, normalization factor C is defined as

713
$$C = \left[\int_{D_{\min}}^{D_{\max}} (D/v)^{k-1} e^{-D/v} dD \right]^{-1}, \quad (11)$$

714 D_{\min} and D_{\max} describe the minimal and maximum particle sizes in the distribution.

715 In order to introduce the vertical inhomogeneity, we use the measurement of snow density and
 716 equivalent optical diameter vertical profiles conducted during the SnowEx17 campaign.
 717 Accounting for that the equivalent optical diameter cannot be directly used to define parameters
 718 of Gamma distribution, we use the vertical profile as a shape of the mode (most frequent value
 719 in a dataset), i.e.

720
$$D_0(z) = \frac{D_e(z)}{D_e(z_{top})} D_0(z_{top}), \quad (12)$$

721 where $D_e(z)$ is the measured vertical profile of equivalent optical diameter, $D_0(z)$ is the vertical
 722 profile of the mode. The mode near the top of snow layer, $D_0(z_{top})$, we assume to be equal 400
 723 μm according to the measurement data reproduced by Saito et al (2019) in Fig. A1.

724 Taking into account the analytical expression of the mode via shape and scale parameters,

725
$$D_0 = (k-1)v. \quad (13)$$

726 and the following relationship between shape and scale parameters derived by Saito et al (2019):

727
$$k = 11.38v^{-0.167} - 2. \quad (14)$$

728 we can estimate parameters k and v of Gamma distribution corresponding to $D_0(z)$ given by Eq
 729 (12).

730 Snow Grain Habit Mixture (SGHM) model is used according to Saito et al (2019). In
 731 particular, the particle habits include droxtal, solid hexagonal column, and solid bullet rosette.
 732 Habit fraction, $f_h(D)$, as a function of maximal dimension of the SGHM model is presented in
 733 the right panel of Fig. 15. The habit fraction is defined so that ,for each D ,

734
$$\sum_{h=1}^3 f_h(D) = 1. \quad (15)$$

735 The selected SGHM model enables us to derive the total volume of ice per unit volume of
 736 air as

$$737 \quad V_t = N \sum_{h=1}^3 \left[\int_{D_{\min}}^{D_{\max}} V_h(D) f_h(D) G(D) dD \right], \quad (16)$$

738 and ice water content (IWC)

$$739 \quad IWC = V_t \rho_{ice}, \quad (17)$$

740 where $V_h(D)$ is the volume of each habit as given in database of Yang and ρ_{ice} is the density of
 741 ice.

742 Taking into account that the vertical profile of IWC is measured (see right panel of Fig.
 743 14), we can obtain the vertical profile of particle number density. Using Eqs (16) and (17), we
 744 have

$$745 \quad N(z) = \frac{IWC(z)}{\rho_{ice} \sum_{h=1}^3 \left[\int_{D_{\min}}^{D_{\max}} V_h(D) f_h(D) G(D, z) dD \right]}. \quad (18)$$

746 Summing up, we define the microphysical properties of snow layer using the following
 747 model of particle size distribution

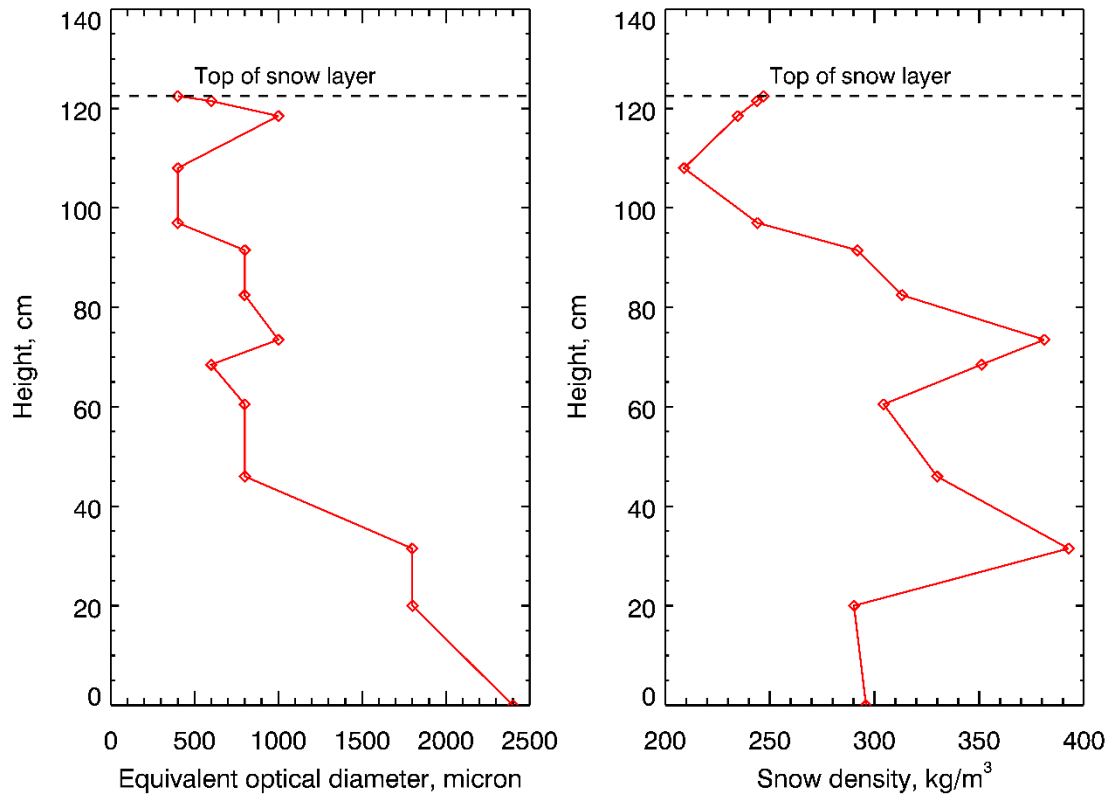
$$748 \quad n(D, z) = N(z) C \left[\frac{(\bar{k} - 1)D}{D_0(z)} \right]^{\bar{k}-1} \exp \left[-\frac{(\bar{k} - 1)D}{D_0(z)} \right], \quad (19)$$

749 where $D_0(z)$ and $N(z)$ are given by Eq (12) and (18), respectively, shape parameter, k , is
 750 assumed to be altitude independent and set to 2.3.

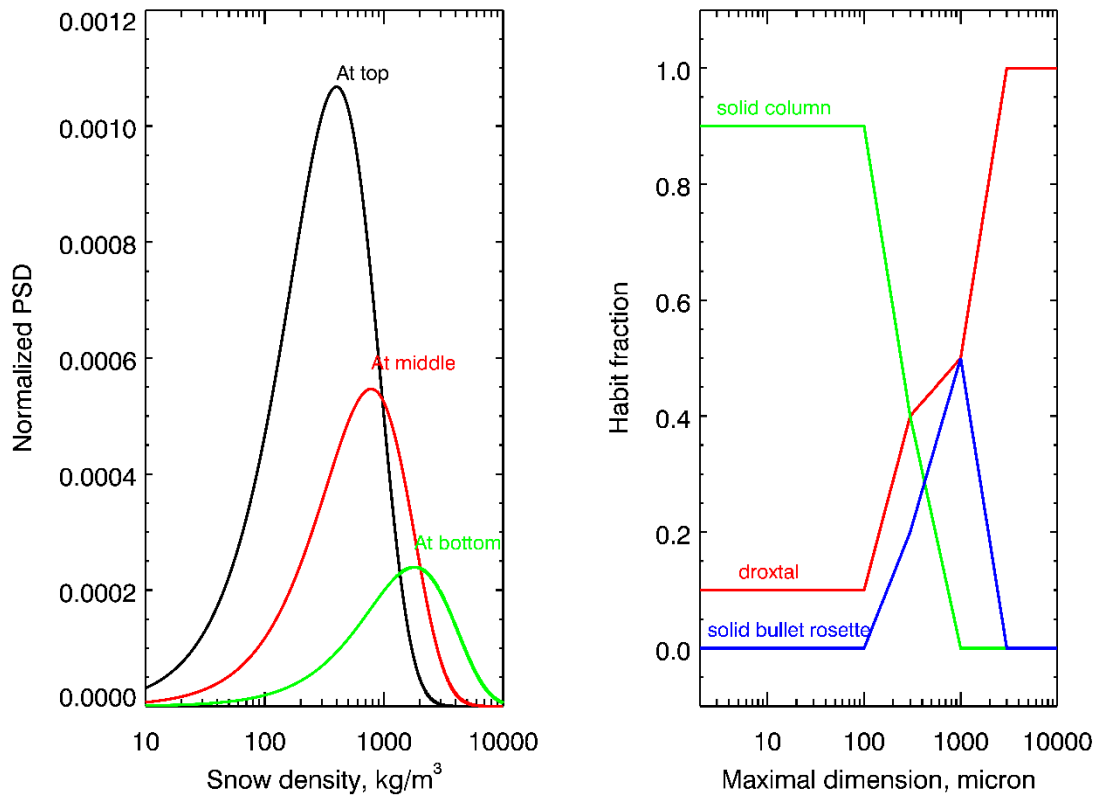
751 The bulk single-scattering properties of snow layer such as extinction coefficient,
 752 scattering coefficient and scattering function are defined by the same way as proposed by Baum
 753 et al. (2011). For instance, the bulk extinction coefficient is calculated as

$$754 \quad \beta_{ext}(z) = \int_{D_{\min}}^{D_{\max}} \left[\sum_{h=1}^3 \sigma_{ext,h}(D) f_h(D) n(D, z) dD \right], \quad (20)$$

755 where $\sigma_{ext,h}(D)$ is the extinction cross-section as given for each habit in database of Yang et
756 al.
757



758
759 Fig. 14 Snow properties used for simulations to investigate the impacts of snow layer
760 model on XBAER retrieval (left) snow grain size profile and (right) snow density observed
761 during SnowEx17 campaign



762

763 Fig. 15 Snow properties used for simulations to investigate the impacts of habit mixture
 764 model on XBAER retrieval: (left) particle size distribution of snow grain size in snow layer;
 765 (right) habit fraction suggested by Saito et al (2019)

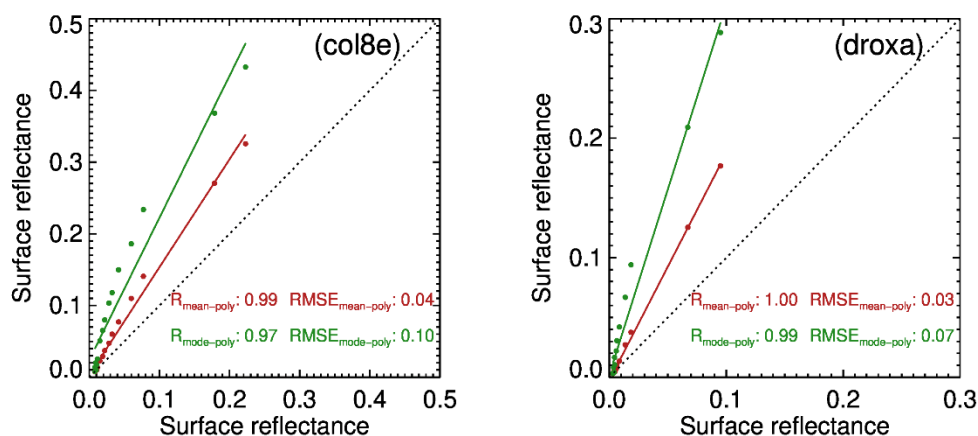
766 The following settings are used to simulate the reference snow reflectance at wavelengths
 767 0.55 and 1.6 μm ;

- 768 ➤ **Snow Layer:** vertically inhomogeneous, polydisperse habit mixture and model as
 769 described above;
- 770 ➤ **Atmosphere:** excluded.

771 Using the simulated reflectances in XBAER algorithm, we have retrieved SPS as dorxtal
 772 with the maximal dimension equal to 740 μm . Taking into account that the model of PSD near
 773 the top of snow layer is 400 μm and the mean value calculated as $kD_0/(k-1)$ is equal to 708 μm ,
 774 one can see that the retrieved maximal dimension is an estimation of mean value of PSD near
 775 the top of snow layer.

776 Since there is no single reference SGS values when a PSD is used, it is important to check
 777 the representativeness of XBAER derived SGS. Accounting for that the mode and mean values
 778 for a given PSD are two typical “effective” way to describe polydisperse medium, we compared
 779 reflectances of snow layer calculated assuming PSD in the form of Gamma distribution and
 780 assuming monodisperse medium with SGS equal to the mode or to the mean of selected PSD.
 781 In order to simplify analysis, we consider vertically homogeneous snow layer consisting of only
 782 single particle habit. The calculations of reflectance were performed for severely roughened
 783 aggregate of 8 columns and droxtal particles setting the shape parameter, k , equal to 2.3 and
 784 the model equal to [100, 300, 500, 700, 1000, 2000, 3000, 5000] μm .

785 Fig. 16 shows the comparison of snow reflectance calculated assuming monodisperse and
 786 polydisperse snow model. In the case of monodisperse model, SGS is assumed to be equal to
 787 the mean or to the mode value of PSD. We can see that the surface reflectance calculated using
 788 the mean value of PSD agrees better with reference values, than reflectance calculated using the
 789 mode value. In particular, the root-mean-square deviation (RMSE) values are more than 2 times
 790 smaller. One can also see from Fig. 16 that the difference between monodisperse reflectances
 791 calculated using mean or mode PSD values decreases with increase of the PSD mode. It can be
 792 explained due to the fact that the increase of PSD mode leads to the increase of absorption and
 793 decrease of reflectance sensitivity with respect to the variation of SGS.



794

795 Fig. 16 The comparison between simulated snow reflectance using mono and poly-disperse
 796 snow model consisting of aggregate of columns (left) and droxtal (right). In the case of

797 monodisperse model, the SGS is assumed to be the mean and mode value of PSD at the top of
798 snow layer (see left panel of Fig. 14). The reference value is shown on the x-axis.

799

800 **8 Conclusions**

801 SGS, SPS, and SSA are three important parameters to describe snow properties. They play
802 important roles in the changes in snow albedo/reflectance and impact the atmospheric and
803 energy-exchange processes. A better knowledge of SGS, SPS, and SSA can provide more
804 accurate information to describe the impact of snow on Arctic amplification processes. The
805 information about SGS, SPS, and SSA may also explore new applications to understand the
806 atmospheric conditions (e.g. aerosol loading). Although some previous attempts (e.g. Lyapustin
807 et al., 2009) show the capabilities of using passive remote sensing to derive SGS over a large
808 scale, no publication has been found to derive SGS, SPS, and SSA simultaneously. To our best
809 knowledge, this is the first paper, attempting to retrieve these parameters using satellite
810 observations.

811 The new algorithm is designed within the framework of the XBAER algorithm. The
812 XBAER algorithm has been applied to derive SGS, SPS, and SSA using the newly launched
813 SLSTR instrument onboard Sentinel-3 satellite. This is the first part of the paper, to describe
814 the algorithm, and to present the sensitivity studies.

815 The SGS, SPS, and SSA retrieval algorithm is based on the recent publication by Yang et
816 al., (2013), in which a database of optical properties for nine typical SPSs (aggregate of 8
817 columns, droxtal, hollow bullet rosettes, hollow column, plate, aggregate of 5 plates, aggregate
818 of 10 plates, solid bullet rosettes, column) are provided. Previous publications show that this
819 database can be used to retrieve ice crystal properties in both ice cloud and snow (e.g., Järvinen
820 et al., 2018; Saito et al., 2019). The algorithm is a LUT-based approach, in which the
821 minimization is achieved by the comparison between atmospherically corrected TOA
822 reflectance at 0.55 and 1.6 μm observed by SLSTR and pre-calculated LUT of surface
823 reflectances under different geometries and snow properties. The retrieval is relatively time-
824 consuming because the minimization has to be performed for each SPS and the optimal SGS

825 and SPS are selected after 9 minimizations are done. The SSA is then obtained using the
826 retrieved SGS and SPS based on another pre-calculated LUT.

827 The sensitivity studies with respect to the impacts of SPS, ICSR, aerosol and cloud
828 contamination on XBAER derived SGS and SPS provide a comprehensive understanding of
829 the retrieval accuracy of the new algorithm. The main findings of the theoretical considerations
830 are: (1) XBAER derived SGS is more likely to represent the average SGS near the top of snow
831 layer when a PSD is known; (2) SPS plays an important role for the retrieval accuracy of SGS,
832 the retrieved SGS can differ several times by usage different SPSs in the retrieval process; (3)
833 Impact of ICSR on the retrieval accuracy of SGS can be neglected, ignoring ICSR completely
834 may introduce maximal 3% error on the retrieval accuracy of SGS, especially for large ice
835 crystals; (4) Assumption of convex particle shape (e.g., sphere) of a non-convex ice crystal
836 leads to the underestimation of the retrieved SSA; (5) The impact of aerosol and cloud increase
837 with the increase of both aerosol/cloud loading and SGS; (6) The impact of instrument SRF
838 may introduce some positive bias for SGS and negative bias for SSA, however, it plays no
839 role for the determination of SPS

840 Even though all major possible factors affecting the retrieval accuracy of XBAER
841 algorithm are investigated in this paper, in reality, the final retrieval accuracy can only be
842 evaluated by performing a thorough comparison with independent measurement results because
843 uncertainties caused by each individual factor can compensate each other in the real satellite
844 retrieval. All details of such validation can be found in the companion paper of Mei et al (2020c).

845

846 **Code and data availability**

847 The code and used dataset can be found at iup.uni-bremen.de/sciatran/

848

849 **Author contributions**

850 LM and VR conceptualized the study, LM, VR and CP implemented the code and processed
851 the data. LM and VR analyzed the data. LM and VR prepared the manuscript with contribution
852 from all co-authors. LM, VR and JB polished the whole manuscript.

853 **Competing interests**

854 The authors declare that they have no conflict of interest.

855

856 **Acknowledgements**

857 This research was funded by the Deutsche Forschungsgemeinschaft (DFG, German Research

858 Foundation) – Project-ID 268020496 – TRR 172. The SLSTR data is provided by ESA. We

859 thank the valuable discussion with Dr. M Saito.

860

861

862

863 **Appendix**

864 According to the definition of specific surface area

865
$$SSA = \frac{A}{\rho V}, \quad (A1)$$

866 one needs to calculate the total area A of ice crystal. In the following sections, we consider

867 in details the basic equations to calculate total area and SSA of different SPSs given in

868 database of Yang et al (2013) and used above within the retrieval algorithm.

869

870 ➤ **Droxtal, solid column, plate**

871 In the case of convex faceted particles such as droxtal, solid column, and plate, the

872 calculation of total area is straightforward and based on the Cauchy's surface area formula:

873
$$A = 4A_p. \quad (A2)$$

874 Taking into account that for selected SPS, one can find corresponding V and A_p in database

875 given by Yang et al., (2013), we have the following results for SSA of such particles:

876
$$SSA = \frac{4A_p}{\rho V}. \quad (A3)$$

877 ➤ **Hollow column**

878 In this case a solid column includes two equal cavities in the form of a hexagonal
 879 pyramid and cannot be considered as convex particle. The aspect ratio of hollow column
 880 with the height, d, of hexagonal pyramid is given according to Yang et al., (2013) as:

881
$$\frac{2a}{L} = \begin{cases} 0.7, & L < 100\mu m \\ \frac{6.96}{\sqrt{L}}, & L \geq 100\mu m \end{cases}, \quad d = 0.25L. \quad (A4)$$

882 The volume of such hollow column is given by

883
$$V = V_c - 2V_p, \quad (A5)$$

884 where the volume of solid column, V_c , and a hexagonal pyramid, V_p , are,

885
$$V_c = \frac{3\sqrt{3}}{2} a^2 L, \quad (A6)$$

886
$$V_p = \frac{\sqrt{3}}{2} a^2 d. \quad (A7)$$

887 Thus, the volume, V, is

888
$$V = \frac{\sqrt{3}}{2} a^2 (3L - 2d). \quad (A8)$$

889 Employing the relationship between d and L given by Eq (A4) and excluding a, we
 890 have

891
$$V = \frac{2.5\sqrt{3}}{2} a^2 L = \begin{cases} m_0 m_1^2 L^3, & L < 100\mu m \\ m_0 m_2^2 L^2, & L \geq 100\mu m \end{cases}, \quad (A9)$$

892 where $m_0 = 2.5 \times \sqrt{3} / 2$, $m_1 = \frac{0.7}{2}$, and $m_2 = \frac{6.96}{2}$. For a selected volume, V , the
 893 length, L , is calculated as follows:

$$894 \quad L = \begin{cases} [V / m_0 / m_1^2]^{\frac{1}{3}}, & V < V_{100} \\ [V / m_0 / m_2^2]^{\frac{1}{2}}, & V \geq V_{100} \end{cases}, \quad (\text{A10})$$

895 where $V_{100} = m_0 m_2^2 100^2$.

896 Let us now calculate the area of each triangle side of the pyramid

$$897 \quad S_t = \frac{a}{2} \sqrt{d^2 + \frac{3a^2}{4}}. \quad (\text{A11})$$

898 The area of lateral surface of two pyramids is

$$899 \quad S_p = 3a\sqrt{4d^2 + 3a^2}. \quad (\text{A12})$$

900 And the total surface area of hollow column is given by

$$901 \quad S = 6aL + 3a\sqrt{4d^2 + 3a^2}, \quad (\text{A13})$$

902 where a and d should be expressed via L according to Eq. (A4).

903 Having obtained the total area, one can calculate specific surface area

$$904 \quad SSA = \frac{S}{\rho V}, \quad (\text{A14})$$

905 ➤ **Hollow bullet rosettes**

906 In this case a solid column includes a cavity in the form of a hexagonal pyramid with
 907 height H and a hexagonal pyramid with height t on the opposite site of column. The aspect
 908 ratio and parameters H and t is given according to Yang et al., (2013) as:

$$909 \quad \frac{2a}{L} = 2.3104L^{-0.37}, \quad t = \frac{\sqrt{3}a}{2 \tan(28^\circ)}, \quad H = 0.5(t + L). \quad (A15)$$

910 The volume of a hollow bullet rosettes is given by

$$911 \quad V_1 = V_c - V_- + V_+. \quad (A16)$$

912 Using Eqs. (A6) and (A7), we have

$$913 \quad V_1 = \frac{3\sqrt{3}}{2} a^2 L - \frac{\sqrt{3}}{2} a^2 H + \frac{\sqrt{3}}{2} a^2 t = \frac{\sqrt{3}}{2} a^2 (3L - H + t). \quad (A17)$$

914 Substituting H as given by Eq (A15), we obtain

$$915 \quad V_1 = \frac{\sqrt{3}a^2}{4} (5L + t). \quad (A18)$$

916 Using Eq (A15), we express parameters a and t of hollow bullet rosettes via L :

$$917 \quad a = m_a L^{p_a}, \quad (A19)$$

$$918 \quad t = m_t m_a L^{p_a}, \quad (A20)$$

919 where coefficients, m_a , m_t , and p_a are

$$920 \quad m_a = \frac{2.3104}{2}, \quad m_t = \frac{\sqrt{3}}{2 \tan(28^\circ)}, \quad p_a = 1 - 0.37. \quad (A21)$$

921 The expression (A18) can be rewritten as:

$$922 \quad V_1 = \frac{\sqrt{3}}{4} m_a^2 L^{2p_a+1} (5 + m_t m_a L^{-0.37}). \quad (A22)$$

923 The total area of hollow bullet rosette is written as

924
$$S_1 = 6aL + \frac{3a}{2} \sqrt{4H^2 + 3a^2} + \frac{3a}{2} \sqrt{4t^2 + 3a^2} \quad (\text{A23})$$

925 and can be calculated when for a selected maximal dimension D the parameter L is
 926 known. For a desired dimension D (volume V) of hollow bullet rosettes, consisting of
 927 6 equal rosettes (See Table 1), Eq (A22) was solved with respect to the length, L, using
 928 following iterative approach:

929
$$L_n = \left[\frac{2V}{3\sqrt{3}m_a^2(5 + m_t m_a L_{n-1}^{-0.37})} \right]^{\frac{1}{2p_a+1}}. \quad (\text{A24})$$

930 The iterative process starts with $L_0=1$ and finishes when $\left| \frac{L_n - L_{n-1}}{L_n} \right| \leq 10^{-4}$. The total
 931 area of hollow bullet rosettes is calculated as;

932
$$S_1 = 6aL + \frac{3a}{2} \sqrt{4H^2 + 3a^2} + \frac{3a}{2} \sqrt{4t^2 + 3a^2}. \quad (\text{A25})$$

933 The SSA is given by

934
$$SSA = \frac{6S_1}{\rho V}. \quad (\text{A26})$$

935 ➤ **Solid bullet rosettes**

936 The aspect ratio and parameter t are given according to Yang et al., (2013) as:

937
$$\frac{2a}{L} = 2.3104L^{-0.37}, \quad t = \frac{\sqrt{3}a}{2 \tan(28^\circ)}. \quad (\text{A27})$$

938 The volume of single solid bullet rosette is

939
$$V_1 = V_c + V_+. \quad (\text{A28})$$

940 Using Eq. (A6), we have

941
$$V_1 = \frac{3\sqrt{3}}{2} a^2 L + \frac{\sqrt{3}}{2} a^2 t = \frac{\sqrt{3}}{2} a^2 (3L + t). \quad (\text{A29})$$

942 Using formula given by Eq (A27), we express parameters a and t of solid bullet rosette
 943 via L :

944
$$a = m_a L^{p_a}, \quad (\text{A30})$$

945
$$t = m_t m_a L^{p_a}, \quad (\text{A31})$$

946 Where coefficients, m_a , m_t , and p_a are the same as in the case of hollow bullet
 947 rosette given by Eq. (A21). The expression (A29) can be rewritten as

948
$$V_1 = \frac{\sqrt{3}}{2} m_a^2 L^{2p_a+1} (3 + m_t m_a L^{-0.37}). \quad (\text{A32})$$

949 For a desired volume V of solid bullet rosettes, consisting of 6 equal rosettes (see
 950 Table 1), this equation was solved with respect to the length, L , of the solid bullet rosette
 951 using following iterative approach:

952
$$L_n = \left[\frac{V}{3\sqrt{3}m_a^2 (3 + m_t m_a L_{n-1}^{-0.37})} \right]^{\frac{1}{2p_a+1}}. \quad (\text{A33})$$

953 The total area of solid bullet rosettes is calculated as;

954
$$S_1 = 6aL + \frac{3\sqrt{3}a^2}{2} + \frac{3a}{2} \sqrt{4t^2 + 3a^2}. \quad (\text{A34})$$

955 The SSA is given by

956
$$SSA = \frac{6S_1}{\rho V}. \quad (\text{A35})$$

957

958 ➤ **Aggregate of 5 and 10 plates**

959 According to the paper of Yang et al (2013), Table 1 provides the aspect ratios of the
 960 ice crystal habits. In the case of an aggregate of columns or plates, the semi-width a and
 961 length L of each hexagonal element of the aggregate are on a relative scale. In order to convert
 962 these parameters in absolute values, let us consider the following relationship given in Yang
 963 et al (2013) for aspect ratio of plate:

$$964 \quad \frac{2a}{L} = \begin{cases} 1, & a \leq 2\mu m \\ m_1 a + m_0, & 2 < a < 5\mu m \\ m a^p, & a \geq 5\mu m \end{cases} \quad (A36)$$

965 where constants are: $m_1=0.2914$, $m_0=0.4172$, $m=0.8038$, $p=0.526$.

966 Using this expression and accounting for that relative values for a , given in Table 1, are
 967 greater than $5\mu m$, we can express L_r via a_r as

$$968 \quad L_r = \frac{2a_r}{m a_r^p} = \frac{2a_r^{1-p}}{m}. \quad (A37)$$

969 where subscript r denotes that they are on relative scale. The volume of a hexagonal plate on
 970 relative scale is given by

$$971 \quad v_r = \frac{3\sqrt{3}}{2} a_r^2 L_r = \frac{3\sqrt{3}}{m} a_r^{3-p}. \quad (A38)$$

972 The volume of aggregates of 5 or 10 plates is given by

$$973 \quad V_r = \frac{3\sqrt{3}}{m} \sum_{i=1}^N a_{r,i}^{3-p}, \quad (A39)$$

974 where $N=5$ and $N=10$ for 5 and 10 plates, respectively. The absolute value of the volume,
 975 V , for a selected maximal dimension of aggregate of 5 or 10 plates one can find in database
 976 presented by Yang et al (2013). Introducing the scaling factor

$$977 \quad C = \frac{V_r}{V}, \quad (A40)$$

978 We rewrite expression (A38) as

$$979 \quad V = \frac{V_r}{C} = \frac{3\sqrt{3}}{mC} \sum_{i=1}^N a_{r,i}^{3-p} = \frac{3\sqrt{3}}{m} \sum_{i=1}^N a_i^{3-p}, \quad (A41)$$

980 where the absolute value of semi-width, a_i , is given by

$$981 \quad a_i = \frac{a_{r,i}}{C^{(3-p)^{-1}}}, \quad (\text{A42})$$

982 Having obtained the absolute value of a_i for each plate, the length L_i is calculated as:

$$983 \quad L_i = \begin{cases} 2a_i, & a \leq 2\mu m \\ \frac{2a_i}{m_1 a_i + m_0}, & 2 < a < 5\mu m \\ \frac{2a^{(1-p)}}{m}, & a \geq 5\mu m \end{cases} \quad (\text{A43})$$

984

985 The total area of a hexagonal plate with semi-width a_i and length L_i is given by

$$986 \quad S_i = 2 \frac{3\sqrt{3}}{2} a_i^2 + 6a_i L_i, \quad (\text{A44})$$

987 The total area is given by

$$988 \quad S = \sum_{i=1}^N S_i. \quad (\text{A45})$$

989 Having obtained the total area, one can calculate SSA as the total surface area of a material per
990 unit of mass:

$$991 \quad SSA = \frac{S}{\rho V}, \quad (\text{A46})$$

992 where $\rho=917 \text{ kg/m}^3$ is the density of ice.

993

994

995

996

997

998

999 Reference

1000 Aoki, T., Fukabori, M., Hachikubo, A., Tachibana, Y., and Nishio, F.: Effects of snow physical parameters on
1001 spectral albedo and bidirectional reflectance of snow surface, *J. Geophys. Res.*, 105(D), 10 219–10 236, 2000.

1002 Baker, I.: Microstructural characterization of snow, firn and ice, *Philosophical Transactions of the Royal Society a-*
1003 *Mathematical Physical and Engineering Sciences*, 377, 10.1098/rsta.2018.0162, 2019.

1004 Battaglia, A., Rustemeier, E., Tokay, A., Blahak, U., and Simmer, C.: PARSIVEL snow observations: a critical
1005 assessment, *J. Atmos. Ocean. Tech.*, 27, 333–344, doi:10.1175/2009JTECHA1332.1, 2010.

1006 Baum, B. A., P. Yang, A. J. Heymsfield, C. Schmitt, Y. Xie, A. Bansemer, Y. X. Hu, and Z. Zhang, Improvements
1007 to shortwave bulk scattering and absorption models for the remote sensing of ice clouds. *J. Appl. Meteor. Clim.*, 50,
1008 1037-1056, 2011

1009 Cauchy, A.: Note sur divers théorèmes relatifs à la rectification des courbes et à la quadrature des surfaces. C.R.
1010 Acad. Sci., 13:1060–1065, 1841.

1011 Chen, N., W. Li, T. Tanikawa, M. Hori, T. Aoki, and K. Stamnes: Cloud mask over snow/ice covered areas for the
1012 GCOM-C1/SGLI cryosphere mission: Validations over Greenland, *J. Geophys. Res. Atmos.*, 119, 12,287-12,300,
1013 doi: 10.1002/2014JD022017, 2014.Colbeck, S. C.: Thermodynamics of snow metamorphism due to variations in
1014 curvature, *J. Glaciol.*, 26, 291-301, 10.3189/S0022143000010832, 1980.

1015 Colbeck, S. C.: Theory of metamorphism of dry snow, *J. Geophys. Res.*, 88, 5475-5482, 1983.

1016 Cole, B. H., Yang, P., Baum, B. A., Riedi, J., and C.-Labonnote, L.: Ice particle habit and surface roughness derived
1017 from PARASOL polarization measurements, *Atmos. Chem. Phys.*, 14, 3739-3750, [https://doi.org/10.5194/acp-14-](https://doi.org/10.5194/acp-14-3739-2014)
1018 3739-2014, 2014.

1019 Cox, S. C., and Munk, W. H. : Measurement of the roughness of the sea surface from photographs of the sun's glitter.
1020 *J. Opt. Soc. Amer.*, 44, 838–850, 1954.

1021 Dietz, A.J., Kuenzer, C., Gessner, U. and Dech, S. : Remote sensing of snow – a review of available methods,
1022 *International Journal of Remote Sensing*, 33:13, 4094-4134, DOI: 10.1080/01431161.2011.640964, 2012.

1023 Domine, F., Gallet, J. C., Barret, M., Houdier, S., Voisin, D., Douglas, T., Blum, J. D., Beine, H., and Anastasio, C.:
1024 The specific surface area and chemical composition of diamond dust near Barrow, Alaska, *J. Geophys. Res.*, 116,
1025 D00R06, 10.1029/2011JD016162 2011.

1026 Domine, F., Picard, G., Morin, S., Barrere, M., Madore, J. B., and Langlois, A.: Major Issues in Simulating Some
1027 Arctic Snowpack Properties Using Current Detailed Snow Physics Models: Consequences for the Thermal Regime
1028 and Water Budget of Permafrost. *Journal of Advances in Modeling Earth Systems*. 11(1), 34-44,
1029 <https://doi.org/10.1029/2018MS001445>,2019

1030 Donahue, C. , Skiles, S.M. and Hammonds, K.: In situ effective snow grain size mapping using a compact
1031 hyperspectral imager. *Journal of Glaciology*, 1–9. <https://doi.org/10.1017/jog.2020.68>,2020.

1032 Dumont, M., Brissaud, O., Picard, G., Schmitt, B., Gallet, J.-C., and Arnaud, Y.: High-accuracy measurements of
1033 snow Bidirectional Reflectance Distribution Function at visible and NIR wavelengths – comparison with modelling
1034 results, *Atmos. Chem. Phys.*, 10, 2507-2520, <https://doi.org/10.5194/acp-10-2507-2010>, 2010.

1035 Flanner, M. G. and Zender, C. S.: Linking snowpack microphysics and albedo evolution, *J. Geophys. Res.*, 111,
1036 D12208, [doi:10.1029/2005JD006834](https://doi.org/10.1029/2005JD006834), 2006.

1037 Frei, A., Tedesco, M., Lee, S., Foster, J., Hall, D. K., Kelly, R., and Robinson, D. A.: A review of global satellite-
1038 derived snow products, *Adv. Space Res., Oceanography, Cryosphere and Freshwater Flux to the Ocean*, 50, 1007–
1039 1029, 2012.

1040 Gallet, J.-C., Domine, F., Zender, C. S., and Picard, G.: Measurement of the specific surface area of snow using
1041 infrared reflectance in an integrating sphere at 1310 and 1550 nm, *The Cryosphere*, 3, 167-182, 2009.

1042 Gardner, A.S. and Sharp, M.J: A review of snow and ice albedo and the development of a new physically based
1043 broadband albedo parameterization, *Journal of Geophysical Research*, 115, F01009, [doi:10.1029/2009JF001444](https://doi.org/10.1029/2009JF001444),
1044 2010Gordon, M. and Taylor, P. A.: The Electric Field During Blowing Snow Events, *Bound-lay. Meteorol.*, 130,
1045 97–115, 2010.

1046 Grenfell, T.C. and Warren, S.G. : Representation of a nonspherical ice particle by a collection of independent spheres
1047 for scattering and absorption of radiation. *J. Geophys. Res.* 104 (D24), 31697–31709.
1048 <http://dx.doi.org/10.1029/1999JD900496>,1999

1049 Hagenmuller, P., Matzl, M., Chambon, G., and Schneebeli, M.: Sensitivity of snow density and specific surface area
1050 measured by microtomography to different image processing algorithms, *The Cryosphere*, 10, 1039–1054,
1051 <https://doi.org/10.5194/tc-10-1039-2016>, 2016.

1052 Hansen, J. and Nazarenko, L.: Soot climate forcing via snow and ice albedos, *Proc. Nat. Acad. Sci.*, 101, 423–428,
1053 2004

1054 Jafariserajehlou, S., Mei, L., Vountas, M., Rozanov, V., Burrows, J. P., and Hollmann, R.: A cloud identification
1055 algorithm over the Arctic for use with AATSR–SLSTR measurements, *Atmos. Meas. Tech.*, 12, 1059–1076,
1056 <https://doi.org/10.5194/amt-12-1059-2019>, 2019.

1057 Järvinen, E., Jourdan, O., Neubauer, D., Yao, B., Liu, C., Andreae, M. O., Lohmann, U., Wendisch, M., McFarquhar,
1058 G. M., Leisner, T., and Schnaiter, M.: Additional global climate cooling by clouds due to ice crystal complexity,
1059 *Atmos. Chem. Phys.*, 18, 15767–15781, <https://doi.org/10.5194/acp-18-15767-2018>, 2018.

1060 Jiao, Z., A. Ding, A. Kokhanovsky, C. Schaaf, F. Bréon, Y. Dong, Z. Wang, Y. Liu, X. Zhang, S. Yin, L. Cui, L.
1061 Mei, Y. Chang: Development of a Snow Kernel to Better Model the Anisotropic Reflectance of Pure Snow into a
1062 Kernel-Driven BRDF Model Framework, *Remote Sensing Environment*, 221, 198-
1063 209, doi:10.1016/j.rse.2018.11.001, 2019.

1064 Jin, Z., Charlock, T. P., Yang, P., Xie, Y., and Miller, W. : Snow optical properties for different particle shapes with
1065 application to snow grain size retrieval and MODIS/CERES radiance comparison over Antarctica. *Remote Sensing*
1066 *of Environment*, 112(9), 3563–3581. doi:10.1016/j.rse.2008.04.011,2008

1067 Kikuchi, K., Kameda, T., Higuchi, K., and Yamashita, A.: A global classification of snow crystals, ice crystals, and
1068 solid precipitation based on observations from middle latitudes to polar regions, *Atmos. Res.*, 132-133, 460–472,
1069 2013.

1070 King, M.D., Platnick, S., Menzel, W.P., Ackerman, S.A., Hubanks, P.A.: Spatial and temporal distribution of clouds
1071 observed by MODIS onboard the Terra and Aqua satellites, *IEEE Trans. Geosci. Remote Sens.* 51 (7), 3826–3852,
1072 2013.

1073 Kokhanovsky, A., Lamare, M.; Danne, O., Brockmann, C., Dumont, M., Picard, G., Arnaud, L., Favier, V., Jourdain,
1074 B.; Le Meur, E., Di Mauro, B., Aoki, T., Niwano, M., Rozanov, V., Korkin, S., Kipfstuhl, S., Freitag, J., Hoerhold,
1075 M., Zühr, A., Vladimirova, D., Faber, A.-K., Steen-Larsen, H.C., Wahl, S., Andersen, J.K., Vandecrux, B., van As,
1076 D., Mankoff, K.D., Kern, M., Zege, E., Box, J.E.: Retrieval of Snow Properties from the Sentinel-3 Ocean and Land
1077 Colour Instrument, *Remote Sens.*, 11, 2280, 2019.

1078 König, M., Winther, J.-G. and Isaksson, E.: Measuring snow and glacier ice properties from satellite, *Reviews of*
1079 *Geophysics*, 39, 1-27, 2001.

1080 Koren, H., Snow grain size from satellite images, SAMBA/31/09, publications.nr.no/5119/Koren_-
1081 _Snow_grain_size_from_satellite_images.pdf, 2009 (last access:7 May, 2018)

1082 Kukla G., Barry, R.G., Hecht, A., Wiesnet, D. eds (1986) SNOW WATCH'85. Proceedings of the workshop held
1083 28-30 October 1985 at the University of Maryland, College Park, MD> Boulder, Colorado, Word Data Center A for
1084 Glaciology (Snow and Ice), *Glaciological Data*, Report GD-18, P 215-223, 1986

1085 Langlois, A., Royer, A., Montpetit, B., Roy, A., and Durocher, M.: Presenting Snow Grain Size and Shape
1086 Distributions in Northern Canada Using a New Photographic Device Allowing 2D and 3D Representation of Snow
1087 Grains. *Frontiers in Earth Science*, 7. doi:10.3389/feart.2019.00347,2020

1088 Legagneux, L. and Domine, F.: A mean field model of the decrease of the specific surface area of dry snow during
1089 isothermal metamorphism, *J. Geophys. Res.*, 110, F04011, <https://doi.org/10.1029/2004JF000181>, 2005.

1090 Legagneux, L., Cabanes, A., and Domine, F.: Measurement of the specific surface area of 176 snow samples using
1091 methane adsorption at 77 K, *J. Geophys. Res.*, 107, 4335, 10.1029/2001jd001016, 2002.

1092 Leroux C., and Fily M. : Modeling the effect of sastrugi on snow reflectance, *J. Geophys. Res.*, 103, 25,779-
1093 25,788, 1998.

1094 Li, W., Stamnes, K., Chen, B., and Xiong, X.: Snow grain size retrieved from near-infrared radiances at multiple
1095 wavelengths, *Geophys. Res. Lett.*, 28, 1699–1702, doi:10.1029/2000GL011641, 2001.

1096 Libois, Q., Picard, G., France, J. L., Arnaud, L., Dumont, M., Carmagnola, C. M., and King, M. D.: Influence of
1097 grain shape on light penetration in snow, *The Cryosphere*, 7, 1803–1818, <https://doi.org/10.5194/tc-7-1803-2013>,
1098 2013.

1099 Liu, J. P., Judith, A. C., Wang, H. J., Song, M. R., and Radley, M. H.: Impact of declining Arctic sea ice on winter
1100 snowfall, *P. Natl. Acad. Sci.*, doi:10.1073/pnas.1114910109, 2012.

1101 Livneh, B., Xia, Y., Mitchell, K. E., Ek, M. B., and Lettenmaier, D. P.: Noah LSM snow model diagnostics and
1102 enhancements, *J. Hydrometeorol.*, 11, 721–738, 2009.

1103 Lyapustin, A., Tedesco, M., Wang, Y.J., Aoki, T., Hori, M. and Kokhanovsky, A. : Retrieval of snow grain size over
1104 Greenland from MODIS, *Remote Sensing of Environment*, 113, 1976-1987,2009.

1105 Mary, A., Dumont, M., Dedieu, J.-P., Durand, Y., Sirguey, P., Milhem, H., Mestre, O., Negi, H. S., Kokhanovsky,
1106 A. A., Lafaysse, M., and Morin, S.: Intercomparison of retrieval algorithms for the specific surface area of snow
1107 from near-infrared satellite data in mountainous terrain, and comparison with the output of a semi-distributed
1108 snowpack model, *The Cryosphere*, 7, 741–761, <https://doi.org/10.5194/tc-7-741-2013>, 2013.

1109 McFarlane, S. A., Marchand, R. T., and Ackerman, T. P.: Retrieval of cloud phase and crystal habit from Multiangle
1110 Imaging Spectroradiometer (MISR) and Moderate Resolution Imaging Spectroradiometer (MODIS) data, *J.*
1111 *Geophys. Res.-Atmos.*, 110, D14201, doi:10.1029/2004JD004831, 2005.

1112 Mei, L.L., Xue, Y., de Leeuw, G., von Hoyningen-Huene, W., Kokhanovsky, A.A., Istomina, L., Guang, J., Burrows,
1113 J. P.: Aerosol Optical depth retrieval in the Arctic region using MODIS over snow. *Remote Sensing of Environment*.
1114 128,234 -245, 2013a.

1115 Mei, L.L., Xue, Y., von Hoyningen-Huene, W., Istomina, L., Kokhanovsky, A.A., de Leeuw, G., Guang, J., Burrows,
1116 J. P.: Aerosol Optical depth retrieval over snow using AATSR data. *International Journal of Remote Sensing*. 34(14),
1117 5030 – 5041, 2013b.

1118 Mei, L. L., Rozanov, V., Vountas, M., Burrows, J., Levy, R., Lotz, W.: A Cloud masking algorithm for the XBAER
1119 aerosol retrieval using MERIS data. *Remote Sensing of Environment*. 197, 141-160,
1120 <http://dx.doi.org/10.1016/j.rse.2016.11.016>, 2017.

1121 Mei, L., Vandembussche, S., Rozanov, V., Proestakis, E., Amiridis, V., Callewaert, S., Vountas, M., Burrows, J. P.,
1122 2020, On the retrieval of aerosol optical depth over cryosphere using passive remote sensing, *Remote Sensing of*
1123 *Environment*, 241, 111731, <https://doi.org/10.1016/j.rse.2020.111731>, 2020a.

1124 Mei, L.L., Rozanov, V., Ritter, C., Heinold, B., Jiao, Z.T., Vountas, M., Burrows, J.P.: Retrieval of aerosol optical
1125 thickness in the Arctic snow-covered regions using passive remote sensing: impact of aerosol typing and surface
1126 reflection model. *IEEE Transactions on Geoscience and Remote Sensing*. 10.1109/TGRS.2020.2972339, 1-15.
1127 2020b.

1128 Mei, L., Rozanov, V., Jäkel, E., Cheng, X., Vountas, M., and Burrows, J. P.: The retrieval of snow properties from
1129 SLSTR/Sentinel-3 – part 2: results and validation, *The Cryosphere Discuss.* [preprint], <https://doi.org/10.5194/tc->

- 1130 2020-270, in review, 2020c. Mishchenko MI, Travis LD, Lacis AA. Scattering, absorption, and emission of light by
1131 small particles. Cambridge University Press; 2002.
- 1132 Nakaya, U., Sekido, Y., General classification of snow crystals and their frequency of occurrence. J. Fac. Sci.,
1133 Hokkaido Imperial Univ., Ser. II I-9, 234–264, 1938
- 1134 Nakaya, U.: Snow Crystals: Natural and Artificial, Harvard Univ. Press, Cambridge, 1954.
- 1135 Painter, T. H., Dozier, J., Roberts, D. A., Davis, R. E., and Greene, R. O.: Retrieval of subpixel snow-covered area
1136 and grain size from imaging spectrometer data, *Remote Sens. Environ.*, 85, 64–77, 2003.
- 1137 Painter, T.H., Rittger, K., McKenzie, C., Slaughter, P., Davis, R.E., Dozier, J.: Retrieval of subpixel snow covered
1138 areas, grain size, and albedo from MODIS, *Remote Sensing of Environment*, 113, 868-879, 2009.
- 1139 Peltoniemi, J., Hakala, T., Suomalainen, J., & Puttonen, E.: Polarised bidirectional reflectance factor measurements
1140 from soil, stones, and snow. *Journal of Quantitative Spectroscopy and Radiative Transfer*, 110(17), 1940-1953, 2009
- 1141 Platnick, S., Meyer, K. G., King, M. D., Wind, G., Amarasinghe, N., Marchant, B., Arnold, G. T., Zhang, Z.,
1142 Hubanks, P. A., Holz, R. E., Yang, P., Ridgway, W. L., and Riedi, J.: The MODIS Cloud Optical and Microphysical
1143 Products: Collection 6 Updates and Examples From Terra and Aqua, *IEEE Trans. Geosci. Remote*, 55, 502–525,
1144 2017
- 1145 Picard, G., Arnaud, L., Domine, F., and Fily, M.: Determining snow specific surface area from near-infrared
1146 reflectance measurements: Numerical study of the influence of grain shape. *Cold Regions Science and Technology*,
1147 56(1), 10–17. doi:10.1016/j.coldregions.2008.10.001, 2009.
- 1148 Pirazzini, R., Räisänen, P., Vihma, T., Johansson, M., and Tastula, E.-M.: Measurements and modelling of snow
1149 particle size and shortwave infrared albedo over a melting Antarctic ice sheet, *The Cryosphere*, 9, 2357-2381,
1150 <https://doi.org/10.5194/tc-9-2357-2015>, 2015.
- 1151 Pohl, C., Istomina, L., Tietsche, S., Jäkel, E., Stapf, J., Spreen, G., and Heygster, G.: Broadband albedo of Arctic
1152 sea ice from MERIS optical data, *The Cryosphere*, 14, 165–182, <https://doi.org/10.5194/tc-14-165-2020>, 2020a.

1153 Pohl C., Rozanov V.V. , Mei L. , Burrows J.P., Heygster G. and Spreen G.: Implementation of an ice crystal single-
1154 scattering property database in the radiative transfer model SCIATRAN, *J. Quant. Spectrosc. Radiat. Transfer*,
1155 doi: <https://doi.org/10.1016/j.jqsrt.2020.107118>, 2020b

1156 Pope A., Gareth Rees, W., Fox, A.J. and Fleming, A.: Open access data in polar and cryo spehric remote sensing,
1157 *Remote sensing*, 6, 6183-6220, 2014.

1158 Qu, Y., Liang, S.L., Liu, Q., He, T., Liu, S.H. and Li ,X.W.: Mapping surface broadband albedo from satellite
1159 observations: A review of literatures on algorithms and products, *Remote sensing*, 7, 990-1020, 2015.

1160 Räisänen, P., Kokhanovsky, A., Guyot, G., Jourdan, O., and Nousiainen, T.: Parameterization of single-scattering
1161 properties of snow, *The Cryosphere*, 9, 1277–1301, <https://doi.org/10.5194/tc-9-1277-2015>, 2015.

1162 Räisänen, P., Makkonen, R., Kirkevåg, A., and Debernard, J. B.: Effects of snow grain shape on climate simulations:
1163 sensitivity tests with the Norwegian Earth System Model, *The Cryosphere*, 11, 2919-2942,
1164 <https://doi.org/10.5194/tc-11-2919-2017>, 2017.

1165 Rozanov, V. V., Rozanov, A. V., Kokhanovsky, A. A., and Burrows, J. P.: Radiative transfer through terrestrial
1166 atmosphere and ocean: Software package SCIATRAN, *J. Quant. Spect. Rad. Trans.* 133, 13–71, doi:10.5194/acp-
1167 8-1963-2008, 2014.

1168 Saito, M., P. Yang, N. G. Loeb, and S. Kato: A novel parameterization of snow albedo based on a two-layer snow
1169 model with a mixture of grain habits, *J. Atmos. Sci.*, 76, 1419–1436, 2019.

1170 Satellite Snow Monitoring Community (SSMC), Perspectives for a European Satellite-based Snow Monitoring
1171 Strategy, White Paper, *Satellite Snow Monitoring Community*, ESA DUE GlobSnow-2 Consortium, 2014.

1172 Schneider, A., Flanner, M., De Roo, R., and Adolph, A.: Monitoring of snow surface near-infrared bidirectional
1173 reflectance factors with added light-absorbing particles, *The Cryosphere*, 13, 1753–1766, <https://doi.org/10.5194/tc->
1174 13-1753-2019, 2019.

1175 Serreze, M. C. and Francis, J. A.: The Arctic amplification debate, *Climatic Change*, 76, 241–264, 2006.

1176 Sinnhuber, B.-M., Sheode, N., Sinnhuber, M., Chipperfield, M. P., Feng, W.:The contribution of anthropogenic
1177 bromine emissions to past stratospheric ozone trends: a modelling study. *Atmos. Chem. Phys.* 9, 2863-2871,
1178 <https://doi.org/10.5194/acp-9-2863-2009>, 2009.

1179 Stamnes, K., Li, W., Eide, H., Aoki, T., Hori, M. and Storvold, R.: ADEOSII/GLI snow/ice products - part I:
1180 Scientific basis, *Remote Sens. Environ.*, 111, 258–273, doi:10.1016/j.rse.2007.03.023, 2007.

1181 Taillandier, A. S., Domine, F., Simpson, W. R., Sturm, M., and Douglas, T. A.: Rate of decrease of the specific
1182 surface area of dry snow: Isothermal and temperature gradient conditions, *J. Geophys. Res.*, 112, F03003,
1183 10.1029/2006jg000514, 2007.

1184 Tsukerman, E. and Veomett, E. : A Simple Proof of Cauchy's Surface Area Formula, *arXiv*, 1604.05815, 2016

1185 Ulanowski, Z., Kaye, P. H., Hirst, E., Greenaway, R. S., Cotton, R. J., Hesse, E., and Collier, C. T.: Incidence of
1186 rough and irregular atmospheric ice particles from Small Ice Detector 3 measurements, *Atmos. Chem. Phys.*, 14,
1187 1649-1662, 10.5194/acp-14-1649-2014, 2014.

1188 Tomasi, C., Kokhanovsky, A. A., Lupi, A., Ritter, C., Smirnov, A., O'Neill, N. T., Stone, R. S., Holben, B. N., and
1189 Nyeki, S.: Aerosol remote sensing in polar regions, *Earth-Sci. Rev.*, 140, 108–157,
1190 doi:10.1016/j.earscirev.2014.11.001, 2015.

1191 Van de Hulst, H :Light Scattering by Small Particles, Dover Publications, 496 pages, 1981

1192 Warren, S. and Wiscombe, W.: A model for the spectral albedo of snow, II: Snow containing atmospheric aerosols,
1193 *J. Atmos. Sci.*, 37, 2734–2745, 1980.

1194 Wiebe, H., Heygster, G., Zege, E., Aoki, T., and Hori, M.: Snow grain size retrieval SGSP from optical satellite data:
1195 Validation with ground measurements and detection of snow fall events, *Remote Sens. Environ.*, 128, 11–20,
1196 <https://doi.org/10.1016/j.rse.2012.09.007>, 2013.

1197 Xiong, C., & Shi, J.: Snow specific surface area remote sensing retrieval using a microstructure based reflectance
1198 model. *Remote Sensing of Environment*, 204, 838–849. doi:10.1016/j.rse.2017.09.017, 2018

- 1199 Yamaguchi, S., Ishizaka, M., Motoyoshi, H., Nakai, S., Vionnet, V., Aoki, T., Yamashita, K., Hashimoto, A., and
1200 Hachikubo, A.: Measurement of specific surface area of fresh solid precipitation particles in heavy snowfall regions
1201 of Japan, *Cryosphere*, 13, 2713-2732, 10.5194/tc-13-2713-2019, 2019.
- 1202 Yang, P., Bi, L., Baum, B. A., Liou, K.-N., Kattawar, G. W., Mishchenko, M. I. And Cole, B.: Spectrally consistent
1203 scattering, absorption, and polarization properties of atmospheric ice crystals at wavelengths from 0.2 to 100 μm , *J.*
1204 *Atmos. Sci.* 70, 330–347, 2013.
- 1205